SECURITY INFORMATION

NACA
RM-L52B06

53
Copy 1
RM L52B06

UNCLASSIFIED

CONFIDENTIAL

NACA RM L52B06

Classification Changed to
UNCLASSIFIED
NACA Research Abstracts #44
dated 6/12/53 (4/13/53)
Date 7/17/53
By J. E. Newlan

NACA

RESEARCH MEMORANDUM

CASE FILE
COPY

APPLICATION OF SUPERSONIC VORTEX-FLOW THEORY TO THE DESIGN OF SUPERSONIC IMPULSE COMPRESSOR- OR TURBINE-BLADE SECTIONS

By Emanuel Boxer, James R. Sterrett, and John Wlodarski

Langley Aeronautical Laboratory
Langley Field, Va.

JPL LIBRARY
CALIFORNIA INSTITUTE OF TECHNOLOGY

MAY 2 1952

CLASSIFIED DOCUMENT

This material contains information affecting the National Defense of the United States within the meaning of the espionage laws, Title 18, U.S.C., Secs. 793 and 794, the transmission or revelation of which in any manner to an unauthorized person is prohibited by law.

NATIONAL ADVISORY COMMITTEE
FOR AERONAUTICS
WASHINGTON
April 24, 1952

CONFIDENTIAL

UNCLASSIFIED

Classification Changed to
UNCLASSIFIED
NACA Research Abstracts #44
dated 6/12/53 (4/13/53)
Date 7/17/53 By D. E. Nevolan
NCA

NATIONAL ADVISORY COMMITTEE FOR AERONATUICS

RESEARCH MEMORANDUM

APPLICATION OF SUPERSONIC VORTEX-FLOW THEORY TO THE DESIGN OF SUPERSONIC IMPULSE COMPRESSOR- OR TURBINE-BLADE SECTIONS

By Emanuel Boxer, James R. Sterrett, and John Wlodarski

SUMMARY

A method for designing shock-free supersonic impulse compressor and turbine blades in which the blade passage is essentially the space between two concentric circles is presented. Since the shock-free supersonic flow between two concentric circles is a vortex flow, the problem is one of designing an entrance to the circular-arc passage which will convert the uniform entering flow to the required vortex distribution and vice versa at the exit. The coordinates of many transition arcs have been computed and are included in tabular form. The resulting sections are all related to one another so that changes in the design variables can be investigated independently in cascade and the performance of a section for particular rotor conditions may be deduced from tests of representative sections.

Three methods of increasing the thickness, particularly near the leading and trailing edges, are presented although not experimentally investigated. The passage shape was investigated for its ability to start supersonically and the maximum design inlet Mach number for starting was determined for given vortex-blade parameters.

Cascade test results of four blade passages designed to turn the flow 120° at an inlet Mach number of 1.57 showed reasonable agreement with predicted surface static pressures. The stagnation pressure recovery was approximately 87.5 percent for all sections.

INTRODUCTION

At the turn of the century, the newly realized potentialities of steam turbines led, among other things, to intensive empirical research into the proper shaping of impulse turbine blades or buckets for use with supersonic inlet velocities. (See reference 1.) The bucket shapes developed at that time, when little was known about supersonic flow other than the existence of the Prandtl-Meyer and Rankine-Hugoniot relations, are still the basis for design of modern impulse steam-turbine buckets since no premium has been placed upon achieving the ultimate in performance.

The present-day revolution in aircraft propulsion has brought about a demand for high-performance compressors and turbines and has instigated an intensive research in the field of high-pressure-ratio compressors and turbines with large flow-handling capacities, small frontal area, light weight, and high efficiency. With the development of the theory of the supersonic axial-flow compressor by Kantrowitz (reference 2) a new field of great promise in compressor research was opened. In particular, the entirely supersonic rotor and diffusing stator combination suggested by Kantrowitz and discussed by Ferri (reference 3) holds promise of pressure ratios per stage of 6 to 10 with efficiencies estimated from two-dimensional cascade tests to be between 70 and 80 percent. Part of the problem to be overcome for compressors of this type is the design of efficient rotor-blade sections to turn the air supersonically through large angles with very little or no reaction (that is, static-pressure rise), a requirement identical to that for efficient impulse turbine buckets. The understanding of supersonic flow has progressed rapidly in recent years. Liccini (reference 4) has demonstrated that turning passages very much more efficient than those cited by Stodola are now possible. The analytical determination of the blade shape for each design by the graphical characteristic method of solution and check testing in cascade, however, is laborious. The purpose of this paper is to present an anlytical method for the design of two-dimensional related sections such that the selection of a blade for particular rotor conditions may be made quickly and easily and its performance deduced from tests of representative sections in cascade.

The principal part of the turning, in what are called vortex impulse sections, is accomplished by concentric streamlines with a vortex-type distribution of velocity for which an analytical potential-flow solution of the equation of the characteristic or Mach lines has been developed by A. Busemann. A transition section at the leading part is used to set up this vortex flow and is duplicated at the rear of the symmetrical blade to return the flow to the required uniform exit condition. The resulting sections are related to one another so that changes in the design variables, that is, design inlet and exit Mach number, blade surface Mach numbers, and turning angles can be investigated independently in cascade. Inasmuch as most practical vortex sections contract the flow, it was necessary to investigate analytically the supersonic starting problem. In addition, several methods of thickening the vanishingly thin leading and trailing edges which are a result of the assumption of shock-free flow are suggested for practical compressor-blade application.

The effects of the boundary layer upon the potential-flow solution were obtained experimentally by several cascade tests of typical impulse blade sections at an inlet Mach number of 1.57.

SYMBOLS

A	area
A^*	area when flow is sonic (for isentropic flow)
a	speed of sound
a^*	speed of sound at point in flow for which the Mach number equals 1.0
C_L	lift coefficient
C_p	specific heat at constant pressure
C	reduction of maximum flow rate due to curvilinear flow
C^*	nondimensional chord (chord/r*)
G^*	nondimensional blade spacing $(2\pi r/nr^*)$
K	nondimensional vortex constant

$$k = \frac{VR^*}{a_o}\sqrt{\frac{\gamma - 1}{2}}$$

M	Mach number (V/a)
M^*	nondimensional velocity ratio (V/a*)
m	rate of mass flow
m/r^*	mass-flow parameter
n	number of blades in a rotor
p	static pressure

P	stagnation pressure
Q	vortex-flow parameter
r	radius from center of rotation of a rotor
r^*	radius of sonic velocity streamline in vortex field
R	radius in vortex field
R^*	nondimensional radius in vortex field (R/r^*)
s	radius ratio (R^*/R_1^*)
t	projection of added thickness normal to axial direction (fig. 9(b))
T	temperature
U	rotational velocity of rotor
u	component of velocity in x direction
v	component of velocity in y direction
V	velocity
V_{max}	maximum velocity of flow for given stagnation conditions $\left(a_o \sqrt{\frac{\gamma - 1}{2}}\right)$
X^*	nondimensional distance in x direction (x/r^*)
Y^*	nondimensional distance in y direction (y/r^*)
β	inlet-flow angle, angle between relative flow and normal to rotor leading edge
γ	ratio of specific heats
δ	leading-edge wedge angle
θ	turning angle
μ	Mach angle
ν	supersonic property angle, angle through which flow must expand from $M = 1.0$ to given Mach number

ψ	ratio of average outlet velocity to inlet velocity
ρ	density
σ	solidity (C^*/G^*)
ϕ	angle between vortex radius vector and x axis, measured positive clockwise
ϕ'	direction of flow in vortex field, measured positive clockwise from x axis
P_3/P_0	stagnation pressure recovery

Subscripts

a	axial direction
e	entrance condition
i	undisturbed inlet condition
l	lower or concave surface
u	upper or convex surface
0	stagnation
s	sonic
2	exit condition

A prime mark denotes conditions after normal shock.

Blade-Section Development

To turn a gas flow through the large angles necessary in supersonic compressor- or turbine-blade passages, a vortex type of flow can be utilized if the inlet surface is properly shaped to convert the uniform inlet velocity into that corresponding to vortex flow and vice versa at the exit. The desirability of using a vortex type of flow is evident when it is realized that the maximum loading for a given peak surface pressure is achieved by uniform upper and lower surface pressures attained through the use of vortex flow. The labor involved in obtaining a solution for a blade profile is reduced because for vortex flow the equation of the Mach lines can be found and, as will be shown, only the transition arcs need to be determined. The fact that the blades so developed are part of a related family is advantageous.

Supersonic vortex-flow theory.- As is well known, (for example, see reference 5), supersonic vortex flow is an irrotational flow the streamlines of which are concentric circles; with a constant velocity along any particular streamline. The velocity in turn varies inversely with radius.

The general vortex equation

$$VR = \text{Constant}$$

can be rewritten

$$M^*R^* = \frac{\text{Constant}}{a^*r^*} = 1.0$$

Restricting the flow to the supersonic realm will limit R^* to values between $\sqrt{\frac{\gamma - 1}{\gamma + 1}}$ and 1.0 with a flow variation shown schematically in figure 1. Since the magnitude of the velocity and its direction is known at any point, the inclination of the Mach waves through any given point may be determined as a function of R^* as shown subsequently.

Since the velocity is normal to the radius (see fig. 2), the Mach wave inclination is $\phi' \pm \mu$ or $\phi + \frac{\pi}{2} \pm \mu$ where

$$\mu = \text{arc sin}\,\frac{1}{M}$$

and

$$M = \sqrt{\frac{2M^{*2}}{(\gamma + 1) - (\gamma - 1)M^{*2}}}$$

so that the Mach wave inclination is $\phi + \frac{\pi}{2} \pm \text{arc sin}\sqrt{\frac{(\gamma + 1)R^{*2} - (\gamma - 1)}{2}}$

The equation of the Mach lines may be found by integration since the slope is a function of ϕ and R^*. The resulting integral equation has been solved in terms of M^*. Rather than develop the direct solution, use may be made of the fact that the Mach lines are characteristic lines and that a functional relation between velocity direction ϕ' and velocity ratio M^* exists along a characteristic line (equations 81 and 89, reference 6). Since $M^* = \frac{1}{R^*}$, the equation of Mach lines can be written in polar form as

$$\phi = \pm\frac{1}{2}\left\{\sqrt{\frac{\gamma + 1}{\gamma - 1}} \text{ arc sin}\left[\frac{(\gamma - 1)}{R^{*2}} - \gamma\right] + \text{arc sin}\left[(\gamma + 1)R^{*2} - \gamma\right]\right\} + \text{Constant}$$

The foregoing development is based upon work done by A. Busemann (unpublished). The Mach wave network in the supersonic vortex field for 4° incremental changes in the value of the constant is shown in figure 3 as originally prepared by Busemann.

Generation of transition arcs.- The flow entering a blade section assumed to be uniform, supersonic, and of constant entropy must be deflected by uniquely shaped boundaries to set up the desired vortex-flow pattern. In the following exposition, it is convenient to discuss the flow in terms of flow direction, ϕ', and the property angle, ν. Tables of functions for two-dimensional flow of a perfect gas have been published in many texts, but, for ready reference, the values of M, M^*, μ, and R^* as functions of ν for $\gamma = 1.40$ are presented in table I.

The inlet value of ν_e must be reduced by means of compression waves to the selected value of ν_l on the concave surface and generally increased through expansions to the value ν_u on the convex surface of the vortex part of the blade. Along a line where $\phi' = 0$, compression waves (shown in fig. 4 as solid lines) have a negative slope and expansion waves (shown dashed), a positive one. The flow (see fig. 4) must be normal to the radial line through the initial point of the most clockwise-spaced concentric arc. Since both surfaces must turn the flow an equal amount,

$$\nu_e - \nu_l + \Delta\phi = \nu_u - \nu_e$$

or

$$\Delta\phi = \nu_l + \nu_u - 2\nu_e$$

where $\Delta\phi$ is the displacement angle between the initial points of the concentric arcs.

If the start of concave circular arc is assumed to be on the y^* axis, then the true vortex flow is bounded by the circular-arc surfaces and the expansion wave through $\phi_l' = 0$ on the concave surface and the compression wave which passes through $\phi_u' = \Delta\phi$ on the convex surface up to their point of intersection. Along these principal characteristic lines (heavier lines in fig. 4), the slope of the crossing characteristic or Mach wave and the flow direction is known at every point. There are expansion waves of total strength $\nu_u - \nu_e$ crossing the principal compression characteristic and total compression wave strength of $\nu_e - \nu_l$ crossing the principal expansion characteristic.

From the theory of characteristics as applied to supersonic flow, the direction and velocity of the flow are known to vary only across a characteristic line. When characteristics are given a finite strength, the solution of a flow problem takes the form of a network of quadrilaterals. The flow parameters within each quadrilateral are assumed constant. Thus, in the present problem, the transition arcs are generated by straight-line elements parallel to the flow within the adjacent quadrilateral or triangle formed by the principal and crossing characteristics and the transition arc itself starting from the circular arcs at $\phi_l' = 0$ and $\phi_u' = \Delta\phi$ and proceeding in the counter-clockwise direction until parallel with the inlet flow. Where necessary, for example, nonsymmetrical sections, the exit transition arcs at the trailing surfaces of the blade are generated in a like manner about a radius labeled $\phi_l' = 0$ with the exception that signs of all flow angles ϕ' are changed.

An illustrative example of a particular design is shown in figure 4 for an assumed inlet ν_e of 8° and ν_l and ν_u equal to 0° and 20°, respectively. In each bounded region of flow there appear two numbers, the upper one of which is the flow direction ϕ', the lower one the property angle ν. The strength of each wave is taken to be 2° so that the transition arc is composed of straight-line elements deflected 2° at the intersection with a characteristic line.

The coordinates of a number of transition arcs obtained algebraically for small increments of ϕ are presented in table II for convex surfaces and in table III for concave surfaces. Each of the arcs originates on the y^* axis for which $\phi' = 0$ and its length is dependent upon the inlet value of ν_e. The range of values of ν_e, ν_l, and ν_u presented is thought to cover foreseeable applications for turbine- or compressor-blade section.

Blade-section layout.- The shape of any particular section is a function of inlet and exit Mach numbers as well as total turning angle and Mach number on the circular-arc surfaces. For a symmetrical profile, the turning angle θ is equal to twice the air inlet angle β_e. The concave and convex circular arcs subtend central angles of $\theta - 2(\nu_e - \nu_l)$ and $\theta - 2(\nu_u - \nu_e)$, respectively.

Once the design parameters have been selected, the flow channel can be constructed quite simply. The circular-arc radius for the selected values of ν_l and ν_u are obtained from table I and the coordinates of the transition arcs are computed from values given in tables II and III transformed by standard trigonometric means through an axis rotation of $\theta/2 + (\nu_l - \nu_e)$ and $\theta/2 + (\nu_e - \nu_u)$ degrees for the concave and convex surfaces, respectively. The convex transition arc is extended by means of a straight line parallel to the inlet or exit flow direction to the rotor leading- or trailing-edge line. To obtain the blade form, the convex surface is displaced a distance G^*, as shown in figure 5, so that the two surfaces are tangent at the leading and trailing edges. Examples of several symmetrical blade sections obtained in this manner are presented in figure 6.

Asymmetric sections may be designed similarly by treating the inlet and exit sections as separate layout problems. To obtain a sharp trailing edge, the exit area normal to the flow can be obtained from the familiar cascade relation

$$\frac{A_2}{A_e} = \frac{\cos \beta_e}{\cos(\beta_e - \theta)}$$

To satisfy the equation of continuity, the design exit value of ν must correspond to that of an isentropic area change A_2/A_e.

Although a flow passage can be constructed for any selection of flow parameters, provided that the sum of transition turning on either surface does not exceed the total turning angle desired, there are solutions for which a compressor- or turbine-blade section does not exist because the surfaces are interchanged resulting in negative thickness. For most practical selections of ν_l, ν_u, and θ, however, no difficulty is encountered.

Not only the blade shape but the solidity σ as well is predetermined by the selection of the surface Mach numbers for a given rotor design. The solidity of a symmetrical blade can be determined analytically without the necessity of graphical construction. The necessary equations to find the solidity of a blade are given in appendix A. Since the mechanical design of a rotor due to blade-hub attachment difficulties as well as the aerodynamic performance depend upon solidity, figures 7 and 8 have been prepared for illustrative purposes. The variation of solidity with turning angles for the case where $\nu_e = \frac{1}{2}(\nu_u + \nu_l)$ and each property angle is constant in turn is presented in figure 7. Figure 8 presents results for the case where the interdependence of the property angles is removed. The lowest solidities are achieved when the divergence of surface Mach numbers or loading is greatest. For preset surface Mach numbers the solidity is affected slightly by a variation of inlet Mach number.

From the aerodynamic standpoint, low solidity is desirable because of lower total frictional losses; however, separation losses and outlet flow-divergence angles will undoubtedly be greater as the pressure rise on the convex surface at the exit transition section becomes greater at low solidities. The designer's selection of a reasonable solidity to yield the highest efficiency is facilitated by the use of vortex sections since the profiles are related to one another and therefore performance estimates may be made by interpolation of the results of cascade tests of representative sections.

Method of Creating Finite Leading-Edge Angle

For use in a practical compressor or turbine the supersonic vortex sections have a serious disadvantage because of the extremely thin leading edges which are subject to rapid wear due to high-velocity solid particles in the stream and to deflection due to the pressure differential existing on the two surfaces. This difficulty may be circumvented by the means outlined subsequently to create a finite wedge angle at the leading and trailing edges.

Subsonic axial velocity component.- Kantrowitz (reference 2) has shown that for subsonic axial velocities when expansion waves are generated along the entrance region (in this case the forepart of the convex surface) an oblique compression shock of strength equal to the total expansion strength will be created to obtain a steady-state condition. A small angle wedge therefore can be placed on the convex surface followed by either an expansion corner as shown in figure 9(a) or a convex arc so placed that all the expansion waves are upstream of the following blade. The expansion waves originating at B and the compression shock from A being of the same family will effectively cancel each other a short distance upstream of the cascade for axial velocities near sonic. The wave pattern in figure 9(a) composed of finite-strength expansion waves is seen to be completely cancelled within the confines of the figure for a group of blades. As in the case of an isolated airfoil in supersonic flow, the waves cancel completely only at an infinite distance from the source of disturbance so that in reality it is only at a great distance from the cascade that the undisturbed Mach number is M_i. As the fluid approaches the cascade it oscillates with increasing amplitude about M_i as a mean. At the entrance the flow is turned and expanded to the inlet value M_e different than M_i to satisfy the equation of continuity.

The graphical procedure used to determine M_i is outlined in reference 2; however, the accuracy of the method is limited and it fails in solving the inverse problem of interest to the compressor designers, namely, that of determining M_e and β_e when M_i and β_i are given.

A simpler method capable of analytic solution is presented. When the oblique shocks are assumed to be relatively weak, the flow process may be regarded as isentropic. The last infinitesimal strength wave in the expansion fan about B to be cancelled (see fig. 9(b)) will be the Mach wave associated with the undisturbed upstream Mach number M_i. If that Mach wave is BD, then a line FD which is tangent at D to the limiting streamline AC entering the passage must be parallel to the direction M_i, and the area normal to the flow across BD is equal to to A_i. The extension of line FD will pass through point E, since a line joining the points E and B is parallel and equal to G*.

Because AC is a streamline and the flow in the expansion fan is isentropic, the change in flow direction $\beta_i - \beta_e$ must equal $\nu_e - \nu_i$ to satisfy the equation of continuity.

To solve the problem analytically, β can be shown to be a function of Mach number since

$$\frac{A_e}{A_i} = \frac{(G^* - t)\cos \beta_e}{G^* \cos \beta_i} = \left(1 - \frac{t}{G^*}\right)\frac{\cos \beta_e}{\cos \beta_i}$$

and

$$\frac{A_e}{A_i} = \frac{A_e}{A^*} \times \frac{A^*}{A_i} = \frac{M_i^*}{M_e^*}\left(\frac{\frac{\gamma + 1}{2} - \frac{\gamma - 1}{2} M_i^{*2}}{\frac{\gamma + 1}{2} - \frac{\gamma - 1}{2} M_e^{*2}}\right)^{\frac{1}{\gamma-1}}$$

Use may be made of the values of ν and $\frac{A}{A^*}$ as a function of Mach number tabulated, for example, in reference 6 to determine the desired unknown through a trial-and-error selection of Mach numbers. Since the solution is a function of t/G^*, the wedge angle is not uniquely determined. Care should be exercised in selecting a suitable angle such that the shock is attached and the position of the expansion corner permits the last wave of the fan to precede the following blade.

Another method utilizes a shock wave originating at the leading edge of the concave surface which will fall inside the passage and therefore will not affect the flow upstream of the leading edge. The value ν_e (see fig. 9(c)) can be obtained from the oblique-shock equations (reference 6) when ν_i and wedge angle δ are known. The points A and B are the start of the transition arcs of a passage designed for an inlet Mach number equivalent to ν_e and for a turning angle $\theta = 2(\beta_i - \delta)$ for a symmetrical section. From the point A, a straight line tangent to the transition arc is projected far enough forward so that the shock wave caused by deflecting the flow at point C intersects the point B on the opposite surface. The line BD is parallel to M_i creating an exterior corner of δ° at B. The basic leading-edge shape for ν_e is indicated by EAF.

From practical considerations, the wedge angle δ should be fairly small to yield a range of rotational speeds for which the shock will be attached as well as alleviating the possible flow separation at B due to shock - boundary-layer interaction.

Supersonic axial-velocity component.- When the axial component of the relative velocity is supersonic, another method of creating a leading-edge wedge is to have the shock originate on the leading edge of the convex surface by taking care to select a wedge angle sufficiently small to insure the shock location within the passage (see fig. 9(d)). The passage in this case is designed for an inlet Mach number equivalent to ν_e and a turning angle $\theta = 2(\beta_i + \delta)$ for a symmetrical section. The surface AC is parallel to the undisturbed inlet velocity M_i and at A the surface is turned sharply to cancel the leading-edge shock. The thinner boundary layer at A, as compared to that at point B (fig. 9(c)) and the centrifugal force will materially aid in preventing flow separation on the concave surface at A. For this reason the performance would be expected to be superior to the second subsonic axial-velocity-component case.

For the symmetrical section, the sharp corners at the trailing edge will give rise to trailing expansion waves and oblique shocks. To a first-order approximation the exit Mach number will equal the entering M_i and the turning angle $\theta = 2\beta_i$ for a true impulse condition.

Consideration of Starting Contraction Ratio

In the design of a passage for supersonic flow, it is important to examine any converging portion to insure that supersonic flow can be started (see reference 7). Most practical vortex sections contract the flow. In this discussion, consideration is given only to those cases when the minimum area occurs between the concentric circular arcs. For given values of ν_l and ν_u it is possible to determine analytically the greatest design value of ν_e for which supersonic flow starts in the passage. The flow can not be assumed one dimensional as in reference 8 because of the large velocity gradient between the channel walls. Since the starting Mach number depends both upon the stagnation-pressure loss through the normal shock and the maximum mass flow through the minimum section, the reduction of mass flow due to curvilinear flow must be obtained. The maximum inlet-design Mach number will therefore be that design value of Mach number for which the maximum rate of flow can be accommodated when the normal-shock loss and the large velocity gradient in the concentric-arc passage are taken into consideration.

When a normal shock is assumed to be spanning the entrance at the instant of starting as shown in figure 10, the gain in entropy through the shock will be constant so that the flow downstream of the shock will still be irrotational. If the circular portion of the passage is sufficiently long, a vortex type of flow will be generated. The vortex equation expressed nondimensionally (developed in appendix B) is

$$\sqrt{\frac{\gamma - 1}{2}}\frac{V}{a_o}s = K = \text{Constant}$$

The immediate problem is to determine the constant $K = K_{max}$ for which the rate of flow is a maximum for a given radius ratio and stagnation conditions. The derivation of the necessary equation is presented in appendix A and the resulting values of K_{max} as a function of the ratio of the concave to convex radius is given in figure 11. The reduction in maximum mass flow C compared to that in a one-dimensional passage of width equal to the distance between the two radii is presented in figure 12.

The mass flow in the passage at the instant of starting when the normal shock spans the inlet is equal to the flow rate when started. The physical area contraction as a function of inlet Mach number and ν_u and ν_l may readily be determined for the started condition. If equated to the maximum contraction ratio for starting, when the flow reduction factor C is taken into consideration the maximum selected value of ν_e, for which the passage can be designed to start, can be found. The derivation of the equations and method of attack are outlined in appendix C. The limiting values of inlet ν_e as a function of ν_l and ν_u calculated as indicated in appendix C are presented in figure 13.

The limiting inlet Mach number, however, is not valid for the thickened leading-edge sections which need to be investigated individually.

Experimental Apparatus and Procedure

The blade models are mounted between glass side walls in the test section of the $2\frac{1}{4}$- by 2-inch supersonic cascade tunnel (fig. 14). This tunnel is a closed-return type in which the flow is produced by a compressor previously used as a supercharger on a V-1650-7 Packard aircraft engine. The power to operate the compressor is furnished by a 300-horsepower direct-current motor. Upstream of the test section is a 24- by 24-inch settling chamber containing three sets of fine screens. Downstream of the test section is a two-dimensional diffuser of approximately 6° divergence angle followed by return ducting incorporating two aircraft type of water-cooled radiators to control the air temperature. An air bleed-off valve in the settling chamber is used to control the settling-chamber pressure at from 1 to approximately 2 atmospheres. All tests herein reported, however, were made with atmospheric stagnation pressure. Schlieren photographs of the flow were made with the use of the usual two parabolic mirror systems.

Two blades forming one passage were used per set. The passage contours are accurately machined to a tolerance of 0.002-inch. In order to gain structural rigidity near the leading and trailing edges, the outer surfaces were arbitrarily designed to have finite edge angles and therefore the blade profiles are not similar nor do they represent any vortex section.

A view of the test section with one sidewall removed is presented in figure 15. The asymmetric supersonic nozzle was designed for an exit Mach number of 1.57 equivalent to a ν of 14°. A solid wood fairing on the convex side and a flexible, adjustable extension on the concave side were used to guide the flow outside of the test passage. The blade models, of $2\frac{1}{4}$-inch span, were mounted on dowel pins press-fitted into bushed holes in one of the glass windows. The angle of attack of the blades could be varied with respect to the nozzle by rotating the glass. In this way the Mach number entering the passage could be varied within limits imposed by the appearance of detached bow waves on the leading edges.

Four sets of blades of different solidities were chosen for testing. Figure 16 is a photograph of one of these blades showing the static-pressure orifices and scratch marks used to create Mach wave disturbances in the flow. All of the blades had a turning angle of 120°. Solidities and the theoretical ν values for the concentric axis and entrance conditions are as follows:

Blade	ν_1 (deg)	ν_u (deg)	ν_e (deg)	Solidity	Figure
I	8	20	14	5.69	6(b)
II	4	24	14	3.64	6(c)
III	0	28	14	2.59	6(a)
IV	0	24	13	2.70	6(e)

In order to prevent the familiar condensation shock phenomenon caused by expanding moist air, the settling-chamber temperature was maintained at a high temperature by manual regulation of the cooling water flow. The operating compressor-pressure ratio for any configuration was obtained by increasing the motor speed until all test section pressures remained unchanged with a further increase in speed. Total and static pressures were measured inside the passage just before the end of the concave blade either by single- or multiple-tube probes. Flow surveys were made at several spanwise stations for several inlet Mach numbers. Chordwise static-pressure orifices were located at the midspan of both passage surfaces. In addition, three spanwise static-pressure orifices on both surfaces were located at the chordwise position where the survey measurements were made. The inlet total pressure and temperature were measured in the settling chamber. All pressure measurements were recorded by photographing a multiple-tube mercury manometer.

RESULTS AND DISCUSSION

The figures and tables presenting the test results for the four passages are tabulated below:

Type of data	Blade			
	I	II	III	IV
	Figure			
Static-pressure distribution	17(a)	17(b)	17(c)	17(d)
Schlieren photographs	19	20	21	22
Total-pressure recoveries	18(a)	18(b)	18(c)	18(d)
	Table			
Weighted average total-pressure recoveries	IV(a)	IV(b)	IV(c)	IV(d)

An examination of the stagnation pressure recoveries at the exit of the blade passages (fig. 18) makes it obvious that the flow is not two dimensional. The boundary layer has "piled up" in toward the center of the convex surface. As in reference 4, there is evidence of circulatory boundary-layer flow down the side wall to the convex surface and inward toward the center of the convex blade. An explanation of this phenomenon can be deduced by a consideration of the centrifugal forces and boundary-layer effects along the side wall. Out in the free stream, the centrifugal force caused by curved streamlines is just balanced by a positive pressure gradient (toward the concave surface). In the wall boundary layer, however, this pressure gradient is greater than the centrifugal force; thus the flow moves down the side walls and inward on the convex surface. For low-aspect-ratio blades such as for these tests, the side-wall boundary-layer inflow effects are felt completely across the span at the exit of the blades. Two-dimensional flow at the spanwise center of the blades could be more closely approached by using large-aspect-ratio blades to minimize the extent of this boundary-layer inflow. The size of the existing equipment, however, prevented the use of large-aspect-ratio blades. In an actual rotor, centrifugal forces also exist in the spanwise direction and therefore the results of these tests should be considered only as conservative indications of the performance of blades in an actual rotor. The fact that the flow is three dimensional in character in these tests should be kept in mind when inspection is made of the schlieren photographs.

An interesting experiment which shows the effect of this boundary-layer inflow was conducted by placing two boundary-layer fences on the convex surface of blade II, placed 1/4 inch from the glass wall. Each fence consisted of a thin plate 1/4 inch high and extending from 10 to 100 percent of the chord. Comparing the pressure recoveries near the convex surface of this modified blade (fig. 18(e)) with the same blade (fig. 18(b)) shows that the fences have reduced boundary-layer accumulation and separation. These particular data should be considered preliminary in nature as static-pressure measurements necessary to correct for shock losses were taken only at the blade surfaces.

Blade I was tested at a slightly higher than design inlet Mach number. This higher inlet Mach number was necessary to prevent shocks in the outer channels, caused by the configuration of the tunnel, from extending ahead of the blades. The static pressures on the surfaces of the blades were higher than design. This effect may be due to the thickening of the boundary layer in this narrow channel. The pressure rise at the rear part of the passage is explained by the slight flow separation on the convex surface as seen from the schlieren photographs (fig. 19(a)), and the consequent diffuser effect due to reduced flow areas.

Static-pressure distributions on passage II are in good agreement with the predicted values except at the rear part of the blade where separation had its usual effect. A study of midspan pressure recoveries indicated a decrease in pressure recovery at the convex wall for an increase of inlet Mach number corresponding to a change of ν_e of 1°, (fig. 18(b)).

Supersonic flow in the passage formed by blade III could not be started at the design inlet Mach number of ν equal to 14°. The inlet Mach number had to be increased to ν value of approximately 18°. Figure 21(a) shows a schlieren photograph of the passage in an unstarted condition. All data presented for this blade were taken at an off-design inlet Mach number. As seen from the schlieren photograph in figure 21(b), the boundary layer separated from the convex blade surface at approximately the 30-percent-chord station, but was apparently reattached a short distance downstream in a manner typical of laminar boundary layer. The usual three-dimensional-flow effects are noted from the schlieren photographs and pressure recoveries.

In figure 13, it can be seen that, for a ν_u of 28° and a ν_l of 0, the maximum design entering Mach number is 14.4°. Blade III, therefore, should start at its design inlet Mach number of ν equal to 14°.

In the derivations of the equations used to plot figure 13, however, the effects of the boundary layer have been neglected. The presence of boundary layer or flow separation would decrease the maximum mass flow, and thus decrease the maximum design entering Mach number. Since blade III was designed with an entering Mach number very close to the limit, it is not surprising that viscosity effects prevented it from starting at a ν of 14°.

The inlet Mach number for blade IV is greater than design by the equivalent of a change in ν of 2°. Nosing down the blades, however, caused the strong shock in the outer bypass channel to extend ahead of the convex-surface blade. Whether this result was caused solely by the tunnel configuration or by the fact that the passage would not start at a lower Mach number was not determined. It should be noted that this blade is designed close to the limiting design maximum inlet Mach number. The static-pressure distribution is in reasonable agreement with predicted values except for the effects of boundary-layer accumulation and separation at the rear of the passage.

The variation of the mass-weighted stagnation-pressure recovery for all blades was small. (See table IV.) An approximate average recovery of 87.5 percent was obtained for all sections tested. Examination of an individual passage shows a large variation of pressure recovery at the various span positions which is caused by three-dimensional flows.

A comparison of the blade loading σC_L for the four blades given indicates that the experimental loading is approximately 90 percent of the theoretical value except for blade number I in which the excellent agreement should be disregarded in view of the marked divergence between predicted and measured pressures.

Blade	σC_L	
	Theoretical	Measured
I	1.77	1.77
II	1.68	1.50
III	1.71	1.54
IV	1.76	1.62

Schlieren photographs shown in figures 19 to 22 give an indication of the flow condition in the blade passages. It is interesting to note in figure 19(c) and figure 22 the close correlation of the theoretical vortex-wave pattern, shown by the dotted line, and the actual resulting waves. The shock waves at the leading edge and in the passage are known to be weak. This weakness is apparent by the rapid dissipation of the downstream reflections and the "roof top" behavior of the boundary layer upon meeting the shock wave on the convex blade surface. This phenomenon is typical of a laminar boundary layer, that is, rapid thickening and separation of the boundary layer upstream of the shock and creation of expansion waves as the boundary layer is rapidly thinned behind the shock. The magnitude of the increased boundary-layer thickness, for such flows, is a function of shock strength (reference 8).

The existence of compression or expansion waves at the exit of the passage can change the boundary layer upstream in the passage, and thus to some extent affect the separated region in the passage. This phenomenon acts much the same as the shock before the head of the total-pressure probe in figure 19(a) which causes the boundary layer to thicken upstream. Although it was impossible with the existing equipment to change the downstream pressure appreciably, the downstream pressure could be varied somewhat by moving the flexible wall. An example of this result is shown in the schlieren photograph in figure 19(c) where the angle of the trailing-edge shock has been changed approximately 10° and the flow leaving the blade is closer to the required exit direction. No appreciable changes were noted in the pressure recovery due to changing the downstream pressure by this method.

The results of the four-blade passages followed similar trends with small variations in over-all results. In general, the discrepancies between theoretical and experimental pressure distributions may be explained by the boundary-layer inflow and flow separation. These two effects acting together caused the pressure to rise in the region of the trailing edge. The data indicate that these discrepancies could be reduced by using suitable devices to minimize the boundary-layer inflow from the side walls. Very little data are available to compare with the present results in order to determine whether the vortex-blade sections are as efficient as any other type. Some data are contained in reference 4, in which a pressure recovery of 95 percent was experienced for a 90° turning passage of solidity 3.12, an inlet Mach number of 1.7, and designed for a static-pressure drop across the blade row. The data are not exactly comparable because of the difference in turning angle, Reynolds number, and aspect ratio. Stodola (reference 1) presents steam-bucket performance in terms of the velocity ratio ψ, which is equal to the ratio of the average outlet velocity to the inlet velocity. The value of ψ from the present tests is approximately 92 percent; whereas the upper limit for the data in reference 1 is about 80 percent when the inlet and outlet static pressure are assumed to be equal.

Moving the concave blade of set I away from the convex blade along the chord bisector line in order to determine what effect misalinement would have on the performance reduced the midspan pressure recovery from 95 to 84 percent for the condition shown in figure 23. The reason for this result is obviously due to the large separation and standing shocks in the passage. The results of this part of the investigation point out the desirability of aerodynamically designing the passage even though the behavior of the boundary layer modified the predicted results.

CONCLUSIONS

A method for designing shock-free supersonic impulse compressor and turbine blades in which the blade passage is essentially the space between two concentric circles is presented. Since the shock-free supersonic flow between two concentric circles is a vortex flow, the problem is one of designing an entrance to the circular-arc passage which will convert the uniform entering flow to the required vortex distribution and vice versa at the exit. The coordinates of many transition arcs have been computed and are included in tabular form. The resulting sections are related to one another so that changes in the design variables can be investigated independently in cascade and the performance of a section for particular rotor conditions may be deduced from tests of representative sections.

Three methods of increasing the thickness particularly near the leading and trailing edges are presented although not experimentally investigated. The ability of the passage to start supersonically was investigated and the limiting design inlet Mach number for starting was determined for given surface Mach numbers.

Four different blade passages designed to turn the flow 120° were investigated in cascade at a Mach number of approximately 1.57. The specific conclusions resulting from such tests are as follows:

1. The chordwise static-pressure distribution agrees reasonably well with design values. The discrepancies are explained by side-wall boundary-layer accumulation and flow separation.

2. The cascade flow was not two dimensional because of the circulatory boundary-layer flow.

3. The weighted stagnation pressure recovery for the entire span is approximately 87.5 percent for all sections.

4. There is little data to indicate whether these pressure recoveries are better or worse than sections differently designed although the recoveries are superior to any of the steam turbine bucket results reported by Stodola.

5. The desirability of aerodynamically designing the passage is borne out by the results obtained when the blades are incorrectly spaced.

Future research on the vortex impulse sections to determine the performance for a range of design variables and effects of leading-edge thickness should be undertaken because of the promising results obtained.

Langley Aeronautical Laboratory
National Advisory Committee for Aeronautics
Langley Field, Va.

APPENDIX A

CALCULATION OF THE SOLIDITY OF A SYMMETRICAL BLADE

The solidity of a symmetrical blade can be determined analytically by using the equations developed in appendix C. Equation (C7b) in appendix C can be rewritten

$$\frac{A_e}{r^*} = \frac{A_e}{A^*} Q\left(R_l^* - R_u^*\right) \tag{A1}$$

From figure 5, it can be seen that

$$G^* = \frac{A_e/r^*}{\sin\left(\frac{\pi}{2} - \beta_e\right)} \tag{A2}$$

or for a symmetrical blade since $\theta = 2\beta_e$

$$G^* = \frac{A_e/r^*}{\cos \theta/2} \tag{A2a}$$

Combining equations (A2a) and (A1)

$$G^* = \frac{A_e}{A^*} \frac{Q\left(R_l^* - R_u^*\right)}{\cos \theta/2} \tag{A3}$$

For a symmetrical blade, the equation of the symmetrical axis (see fig. 5) is

$$X \operatorname{ctn}\left[\theta/2 - \left(\nu_e - \nu_l\right)\right] + Y^* = 0 \tag{A4}$$

where the X^* and Y^* axes are as defined for tables II and III.

The perpendicular distance from this axis to the end point X_l^*, Y_l^* of the concave surface can be shown by analytic geometry to be

$$\frac{C^*}{2} = X_1^* \cos\left[\frac{\theta}{2} - \left(\nu_e - \nu_1\right)\right] + Y_1^* \sin\left[\frac{\theta}{2} - \left(\nu_e - \nu_1\right)\right] \tag{A5}$$

When equations (A3) and (A5) are used, the solidity for a symmetrical blade is thus given by

$$\sigma = \frac{2\left\{X_1^* \cos\left[\frac{\theta}{2} - \left(\nu_e - \nu_1\right)\right] + Y_1^* \sin\left[\frac{\theta}{2} - \left(\nu_e - \nu_1\right)\right]\right\} \cos\frac{\theta}{2}}{\frac{A_e}{A^*} Q\left(R_1^* - R_u^*\right)} \tag{A6}$$

which can be easily solved by using values from table III, (fig. 24) and the values from the following equation which have been published in many texts (for example, reference 6).

$$\frac{A_e}{A^*} = \frac{1}{M_e}\left(\frac{\frac{\gamma - 1}{2} M_e^2 + 1}{\frac{\gamma + 1}{2}}\right)^{\frac{\gamma+1}{2(\gamma-1)}}$$

APPENDIX B

CALCULATION OF THE REDUCTION OF THE MAXIMUM RATE OF MASS FLOW DUE TO CHANNEL-WALL CURVATURE

For most practical cases, the minimum passage width which predetermines the maximum rate of mass flow for given stagnation conditions of pressure and temperature occurs between the concentric circular-arc portions of the throat. When only this curved region of flow is considered, the boundary layer being neglected, an expression may be derived by expressing the reduction in the maximum rate of mass flow due to channel-wall curvature as a function of radius ratio.

When the normal shock spanning the entrance to the blade passage is assumed to be of constant strength (fig. 10) the flow within the passage can be considered irrotational, with a greater entropy than that upstream of the normal shock. For the flow to be irrotational and in radial equilibrium downstream of the shock if bounded by sufficiently long concentric-circular walls, it must satisfy the vortex equation

$$VR^* = \text{Constant} \tag{B1}$$

Since the flow is adiabatic and isentropic

$$\frac{\gamma}{\gamma - 1}\frac{p}{\rho} + \frac{V^2}{2} = \frac{\gamma}{\gamma - 1}\frac{p_o'}{\rho_o'} \tag{B2}$$

and

$$\frac{p}{\rho^\gamma} = \frac{p_o'}{\rho_o'^\gamma} \tag{B3}$$

combining equations (B1), (B2), and (B3) and solving for ρ gives

$$\rho = \rho_o'\left(1 - \frac{\gamma - 1}{2a_o^2}V^2\right)^{\frac{1}{\gamma-1}} = \rho_o'\left(1 - \frac{k^2}{R^{*2}}\right)^{\frac{1}{\gamma-1}} \tag{B4}$$

where $k = \sqrt{\frac{\gamma - 1}{2}}\frac{VR^*}{a_o}$ and ρ_o' equals the stagnation density behind the normal shock.

The mass flow parameter m^* is therefore

$$m^* = \frac{m}{r^*} = \int_{R_u^*}^{R_1^*} \rho V \, dR^* = \int_{R_u^*}^{R_1^*} \rho_o'\left(1 - \frac{k^2}{R^{*2}}\right)^{\frac{1}{\gamma-1}} \sqrt{\frac{2}{\gamma - 1}} \, a_o \frac{k}{R^*} \, dR^* \qquad \text{(B5)}$$

for $\gamma = 1.4$, equation (B5) is reduced to an analytically integrable equation such that

$$m^* = \rho_o'\sqrt{5}\, k a_o \left\{ \frac{\left(R^{*2} - k^2\right)^{7/2}}{5k^2 R^{*5}} - \frac{2}{15} \frac{\left(R^{*2} - k^2\right)^{3/2}}{R^{*3}} - \frac{4}{5} \frac{\left(R^{*2} - k^2\right)^{1/2}}{R^*} - R^* \frac{\left(R^{*2} - k^2\right)^{1/2}}{5k^2} + \log\left[R^* + \left(R^{*2} - k^2\right)^{1/2}\right] \right\}_{R_u^*}^{R_1^*} \qquad \text{(B6)}$$

For all real flows, k is less than R^*. In order to determine k_{max}, that is, that value of k which will yield the maximum rate of flow between R_1^* and R_u^*, equation (B5) is differentiated under the integral sign and equated to zero; thus,

$$\frac{dm^*}{dk} = \rho_o'\sqrt{\frac{2}{\gamma - 1}} \, a_o \int_{R_u^*}^{R_1^*} \left\{ -\frac{2}{\gamma - 1} \frac{k^2}{R^{*3}} \left(1 - \frac{k^2}{R^{*2}}\right)^{\frac{2-\gamma}{\gamma-1}} + \frac{1}{R^*}\left(1 - \frac{k^2}{R^{*2}}\right)^{\frac{1}{\gamma-1}} \right\} dR^* = 0$$

for $\gamma = 1.4$

$$\frac{dm^*}{dk} = \frac{m^*}{k} - \rho_o'\sqrt{5}\, a_o \left[\frac{\left(R^{*2} - k^2\right)^{5/2}}{R^{*5}}\right]_{R_u^*}^{R_1^*} \qquad \text{(B7)}$$

In order to reduce the labor involved in determining the value of k for all possible values of R_l^* and R_u^*, equation (B1) may be made nondimensional.

$$\sqrt{\frac{\gamma - 1}{2}} \frac{V}{a_o} s = K \tag{B8}$$

where

$$s = \frac{R^*}{R_l^*} \qquad s_l = 1.0 \qquad s_u = \frac{R_u^*}{R_l^*} \qquad K = \frac{k}{R_l^*}$$

Equation (B7) is now

$$\left\{\frac{\left(s^2 - K_{max}^2\right)^{7/2}}{5K_{max}s^5} - \frac{\left(s^2 - K_{max}^2\right)^{5/2}}{s^5} - \frac{2}{15} \frac{\left(s^2 - K_{max}^2\right)^{3/2}}{s^3} - \right.$$

$$\frac{4}{5} \frac{\left(s^2 - K_{max}^2\right)^{1/2}}{s} - \frac{s\left(s^2 - K_{max}^2\right)^{1/2}}{5K_{max}^2} +$$

$$\left. \log\left[s + \left(s^2 - K_{max}^2\right)^{1/2}\right]\right\}_{s_u}^{1.0} = 0$$

The resulting values of K_{max} for all possible radius ratios are presented in figure 11.

Equation (B6) may be rewritten

$$m^* = \sqrt{5}\, \rho_o{}' a_o K_{max} \left[\frac{\left(s^2 - K_{max}^2\right)^{5/2}}{s^5}\right]_{s_u}^{1.0} \tag{B9}$$

The maximum one-dimensional mass flow through a passage of width equal to distance between the radii is

$$\rho^*a^*(1 - s_u) = \frac{\rho_o{}'a_o}{\left(1 + \frac{\gamma - 1}{2}\right)^{\frac{1}{\gamma-1}}}\sqrt{\frac{2}{\gamma + 1}}\,(1 - s_u) = 0.5786\rho_o{}'a_o(1 - s_u) \tag{B10}$$

Combining equations (B9) and (B10) to determine the reduction in maximum mass flow C, due to flow curvature

$$C = 1 - 3.8643\,\frac{K_{max}}{1 - s_u}\left[\frac{\left(s^2 - K_{max}{}^2\right)^{5/2}}{s^5}\right]_{s_u}^{1.0} \tag{B11}$$

The value of C is presented in figure 12 as function of s_u.

The position of the sonic radius s_s for any given radius ratio may be found upon substitution of a^* for V in equation (B8). Thus

$$s_s = K_{max}\sqrt{\frac{\gamma + 1}{\gamma - 1}}$$

The sonic radius is very close to the geometric mean radius such that $s_s \approx \sqrt{s_u}$ and may be used to determine K_{max} to a good approximation for gases whose ratios of specific heats are other than 1.4. K_{max} determined by this method is shown dashed in figure 11, and its effect upon mass flow reduction is plotted in figure 12. The maximum error in K_{max} which occurs at the minimum radius ratio for gases of $\gamma = 1.3$, 1.4, and 1.5 is $1\frac{1}{2}$, 2, and $2\frac{1}{2}$ percent, respectively.

APPENDIX C

CALCULATION OF THE MAXIMUM DESIGN ENTERING MACH NUMBER FROM STARTING CONSIDERATIONS

Immediately preceding the starting of a particular passage, a shock will span the inlet. After the shock has passed downstream through the minimum section the rate of mass flow is unaltered. The inlet opening for any Mach number can be obtained when the mass flow through the circular passage is known. The maximum inlet design Mach number for any particular circular passage will therefore be that maximum Mach number for which the maximum rate of flow can be accommodated when the normal-shock loss is taken into consideration.

The rate of mass flow for a developed vortex can be written as

$$\frac{m}{r^*} = \int_{R_u^*}^{R_1^*} \rho V \, dR^* \tag{C1}$$

or

$$\frac{m}{\rho^* a^* r^*} = \int_{R_u^*}^{R_1^*} \frac{\rho V}{\rho^* a^*} \, dR^* = \int_{R_u^*}^{R_1^*} \frac{A}{A^*} \, dR^* \tag{C2}$$

and

$$\frac{A^*}{A} = M^* \left(\frac{\gamma + 1}{2} - \frac{\gamma - 1}{2} M^{*2} \right)^{\frac{1}{\gamma - 1}}$$

and

$$R^* = \frac{1}{M^*}$$

Rewriting equation (C2) gives

$$\frac{m}{\rho^* a^* r^*} = \int_{M_1^*}^{M_u^*} \frac{\left(\frac{\gamma + 1}{2} - \frac{\gamma - 1}{2} M^{*2} \right)^{\frac{1}{\gamma - 1}}}{M^*} \, dM^* \tag{C3}$$

When inlet and vortex flow parameters are equated

$$\frac{m}{\rho^* a^* r^*} = \frac{\rho_e V_e A_e}{\rho^* a^* r^*} = \int_{M_1^*}^{M_u^*} \frac{\left(\frac{\gamma + 1}{2} - \frac{\gamma - 1}{2} M^{*2}\right)^{\frac{1}{\gamma - 1}}}{M^*} dM^* \qquad (C4)$$

or

$$\frac{A_e}{r^*} = \frac{\rho^* a^*}{\rho_e V_e} \int_{M_1^*}^{M_u^*} \frac{\left(\frac{\gamma + 1}{2} - \frac{\gamma - 1}{2} M^{*2}\right)}{M^*} dM^* \qquad (C5)$$

The area contraction is

$$\frac{\frac{A_e}{r^*}}{R_1^* - R_u^*} = \frac{A_e}{r^*}\left(\frac{M_1^* M_u^*}{M_u^* - M_1^*}\right)$$

$$= \frac{\rho^* a^*}{\rho_e V_e} \int_{M_1^*}^{M_u^*} \frac{\left(\frac{\gamma + 1}{2} - \frac{\gamma - 1}{2} M^{*2}\right)^{\frac{1}{\gamma - 1}}}{M^*} dM^* \; \frac{M_1^* M_u^*}{M_u^* - M_1^*} \qquad (C6)$$

Let

$$Q = \frac{M_1^* M_u^*}{M_u^* - M_1^*} \int_{M_1^*}^{M_u^*} \frac{\left(\frac{\gamma + 1}{2} - \frac{\gamma - 1}{2} M^*\right)^{\frac{1}{\gamma - 1}}}{M^*} dM^* \qquad (C7)$$

which is a function of the vortex surface Mach numbers only. For $\gamma = 1.4$

$$Q = \frac{M_1^* M_u^*}{M_u^* - M_1^*}\left[\frac{\left(6 - M^{*2}\right)^{5/2}}{280} + \frac{\left(6 - M^{*2}\right)^{3/2}}{28} - \frac{\left(6 - M^{*2}\right)^{1/2}}{1.555} - 1.571 \log \frac{2.45 + \left(6 - M^{*2}\right)^{1/2}}{M^*}\right]_{M_1^*}^{M_u^*} \qquad (C7a)$$

thus the area contraction is

$$\frac{\rho^* a^*}{\rho_e V_e} Q \tag{C7b}$$

The value of Q is given in figure 24 as a function of ν_l and ν_u.

The starting maximum contraction ratio (from reference 8) is modified by the flow reduction factor C so that starting contraction ratio

$$\text{C.R.} = \frac{P_3}{P_o} \frac{A_e}{A^*}(1 - C) \tag{C8}$$

where $\frac{P_3}{P_o}$ is the total-pressure recovery through a normal shock and $\frac{A_e}{A^*}$ is equal to $\frac{\rho^* a^*}{\rho_e V_e}$ and both are a function of inlet Mach number M_e.

Equating (C7b) and (C8) to determine the maximum design value of M_e such that the contraction is equal to the starting contraction ratio gives

$$\frac{Q}{1 - C} = \frac{P_3}{P_o}$$

Since

$$\frac{P_3}{P_o} = \left(\frac{7}{6} M^2 - \frac{1}{6}\right)^{-2.5} \left(\frac{0.4M^2 + 2}{2.4M^2}\right)^{-3.5}$$

has been tabulated as a function of M in reference 6 the maximum design Mach number for which the section will start can readily be obtained.

REFERENCES

1. Stodola, A.: Steam and Gas Turbines. Vol. I, Peter Smith (New York), 1945.

2. Kantrowitz, Arthur: The Supersonic Axial-Flow Compressor. NACA Rep. 974, 1950. (Formerly NACA ACR L6D02.)

3. Ferri, Antonio: Preliminary Analysis of Axial-Flow Compressors Having Supersonic Velocity at the Entrance of the Stator. NACA RM L9G06, 1949.

4. Liccini, Luke L: Analytical and Experimental Investigation of 90° Supersonic Turning Passages Suitable for Supersonic Compressors or Turbines. NACA RM L9G07, 1949.

5. Sauer, Robert: Introduction to Theoretical Gas Dynamics, J. W. Edwards, Ann Arbor, 1947.

6. Ferri, Antonio: Elements of Aerodynamics of Supersonic Flows. The Macmillan Co., 1949.

7. Kantrowitz, Arthur, and Donaldson, Coleman duP.: Preliminary Investigation of Supersonic Diffusers. NACA ACR L5D20, 1945.

8. Liepmann, H. Wolfgang, Roshko, A., and Dhawan, S.: On Reflection of Shock Waves from Boundary Layers. NACA TN 2334, 1951.

TABLE I

MACH NUMBER, MACH ANGLE AND RADIUS RATIO AS FUNCTION

OF ν FOR $\gamma = 1.40$

ν	μ	M	M*	R*	ν	μ	M	M*	R*
0.0	90.00	1.000	1.000	1.000	15.0	38.55	1.605	1.428	0.7003
.1	79.46	1.017	1.014	.9862	16.0	37.61	1.639	1.448	.6906
.2	76.75	1.027	1.023	.9775	17.0	36.72	1.673	1.467	.6817
.5	72.10	1.051	1.042	.9597	18.0	35.87	1.707	1.486	.6729
1.0	67.57	1.082	1.067	.9372	19.0	35.06	1.741	1.505	.6645
1.5	64.45	1.108	1.088	.9191	20.0	34.29	1.775	1.523	.6566
2.0	62.00	1.133	1.107	.9033	22.0	32.83	1.844	1.559	.6414
2.5	59.95	1.155	1.124	.8897	24.0	31.49	1.915	1.593	.6277
3.0	58.18	1.177	1.141	.8764	25.0	30.85	1.950	1.610	.6211
3.5	56.61	1.198	1.157	.8643	26.0	30.23	1.986	1.627	.6146
4.0	55.20	1.218	1.172	.8532	28.0	29.05	2.059	1.659	.6028
4.5	53.92	1.237	1.186	.8432	30.0	27.96	2.134	1.691	.5914
5.0	52.74	1.257	1.200	.8333	32.0	26.90	2.210	1.722	.5807
6.0	50.62	1.294	1.227	.8150	34.0	25.91	2.289	1.752	.5708
7.0	48.75	1.330	1.252	.7987	35.0	25.43	2.329	1.767	.5659
8.0	47.08	1.366	1.277	.7831	36.0	24.96	2.369	1.781	.5615
9.0	45.57	1.400	1.300	.7692	38.0	24.07	2.452	1.810	.5525
10.0	44.18	1.435	1.323	.7559	40.0	23.21	2.538	1.838	.5441
11.0	42.89	1.469	1.345	.7435	45.0	21.21	2.764	1.905	.5249
12.0	41.70	1.503	1.367	.7315	50.0	19.39	3.013	1.967	.5084
13.0	40.58	1.537	1.388	.7205	55.0	17.71	3.287	2.025	.4938
14.0	39.54	1.571	1.408	.7102	60.0	16.16	3.594	2.080	.4808

TABLE II

COORDINATES OF TRANSITION SECTIONS FOR CONVEX BLADE PASSAGE $\gamma = 1.40$

$-\phi$	ν_e	$-X^*$	Y^*
$\nu_u = 40^\circ$			
0	40	0	0.5441
1	39	.0186	.5439
2	38	.0370	.5434
3	37	.0549	.5426
4	36	.0724	.5416
5	35	.0894	.5402
6	34	.1061	.5386
7	33	.1226	.5368
8	32	.1388	.5346
9	31	.1546	.5323
10	30	.1701	.5297
11	29	.1855	.5268
12	28	.2007	.5238
13	27	.2156	.5205
14	26	.2304	.5169
15	25	.2450	.5132
16	24	.2593	.5092
17	23	.2735	.5050
18	22	.2876	.5005
19	21	.3014	.4959
20	20	.3151	.4911
21	19	.3286	.4860
22	18	.3419	.4808
23	17	.3551	.4753
24	16	.3706	.4686
25	15	.3859	.4616
26	14	.3959	.4569
27	13	.4056	.4520
28	12	.4176	.4458
29	11	.4293	.4394
30	10	.4407	.4330
31	9	.4517	.4265
32	8	.4622	.4201
33	7	.4720	.4138
34	6	.4810	.4079
$\nu_u = 38^\circ$			
0	38	0	0.5525
1	37	.0190	.5523
2	36	.0375	.5519
3	35	.0556	.5511
4	34	.0734	.5500
5	33	.0908	.5486
6	32	.1080	.5470
7	31	.1247	.5451
8	30	.1410	.5429
9	29	.1572	.5405
10	28	.1732	.5378
11	27	.1889	.5349
12	26	.2043	.5318
13	25	.2196	.5284
14	24	.2346	.5248
15	23	.2495	.5209
16	22	.2642	.5169
17	21	.2786	.5126
18	20	.2928	.5081
19	19	.3069	.5034
20	18	.3208	.4985
21	17	.3346	.4933
22	16	.3481	.4880
23	15	.3614	.4825
24	14	.3745	.4768
25	13	.3872	.4710
26	12	.3997	.4650
27	11	.4120	.4589
28	10	.4238	.4528
29	9	.4353	.4466
30	8	.4462	.4404
31	7	.4565	.4343
32	6	.4660	.4285
$\nu_u = 36^\circ$			
0	36	0	0.5614
1	35	.0191	.5612
2	34	.0380	.5607
3	33	.0565	.5599
4	32	.0746	.5588
5	31	.0924	.5574
6	30	.1097	.5558
7	29	.1268	.5538
8	28	.1436	.5516
9	27	.1601	.5491
10	26	.1764	.5464
11	25	.1924	.5435
12	24	.2082	.5403
13	23	.2237	.5368
14	22	.2391	.5331
15	21	.2542	.5292
16	20	.2690	.5251
17	19	.2838	.5207
18	18	.2983	.5162
19	17	.3126	.5114
20	16	.3267	.5064
21	15	.3406	.5012
22	14	.3542	.4958
23	13	.3675	.4903
24	12	.3806	.4846
25	11	.3934	.4788
26	10	.4058	.4729
27	9	.4177	.4669
28	8	.4291	.4610
29	7	.4399	.4551
30	6	.4499	.4495
$\nu_u = 34^\circ$			
0	34	0	0.5707
1	33	.0196	.5705
2	32	.0389	.5700
3	31	.0577	.5692
4	30	.0761	.5681
5	29	.0942	.5667
6	28	.1119	.5650
7	27	.1293	.5630
8	26	.1464	.5607
9	25	.1633	.5582
10	24	.1798	.5555
11	23	.1961	.5524
12	22	.2122	.5492
13	21	.2277	.5457
14	20	.2433	.5420
15	19	.2591	.5379
16	18	.2742	.5337
17	17	.2892	.5293
18	16	.3039	.5246
19	15	.3184	.5198
20	14	.3327	.5147
21	13	.3466	.5095
22	12	.3602	.5042
23	11	.3736	.4986
24	10	.3865	.4930
25	9	.3990	.4873
26	8	.4110	.4816
27	7	.4223	.4759
28	6	.4328	.4705
$\nu_u = 32^\circ$			
0	32	0	0.5807
1	31	.0199	.5805
2	30	.0395	.5800
3	29	.0587	.5792
4	28	.0775	.5781
5	27	0.0959	0.5766
6	26	.1140	.5749
7	25	.1318	.5728
8	24	.1492	.5705
9	23	.1664	.5680
10	22	.1833	.5651
11	21	.2000	.5621
12	20	.2163	.5587
13	19	.2325	.5552
14	18	.2484	.5513
15	17	.2640	.5473
16	16	.2795	.5432
17	15	.2945	.5389
18	14	.3093	.5342
19	13	.3239	.5293
20	12	.3382	.5242
21	11	.3522	.5190
22	10	.3658	.5137
23	9	.3789	.5082
24	8	.3915	.5027
25	7	.4035	.4973
26	6	.4146	.4920
$\nu_u = 30^\circ$			
0	30	0	0.5913
1	29	.0203	.5911
2	28	.0403	.5906
3	27	.0598	.5898
4	26	.0792	.5886
5	25	.0980	.5871
6	24	.1163	.5854
7	23	.1344	.5833
8	22	.1522	.5809
9	21	.1697	.5783
10	20	.1869	.5754
11	19	.2039	.5723
12	18	.2207	.5689
13	17	.2371	.5652
14	16	.2533	.5614
15	15	.2692	.5573
16	14	.2848	.5529
17	13	.3001	.5484
18	12	.3150	.5437
19	11	.3297	.5388
20	10	.3433	.5340
21	9	.3570	.5288
22	8	.3710	.5233
23	7	.3835	.5181
24	6	.3953	.5131
$\nu_u = 28^\circ$			
0	28	0	0.6026
1	27	.0207	.6024
2	26	.0411	.6019
3	25	.0611	.6010
4	24	.0806	.5998
5	23	.0998	.5983
6	22	.1186	.5965
7	21	.1372	.5944
8	20	.1553	.5920
9	19	.1732	.5894
10	18	.1908	.5864
11	17	.2081	.5832
12	16	.2251	.5797
13	15	.2418	.5760
14	14	.2582	.5721
15	13	.2743	.5679
16	12	.2900	.5636
17	11	.3054	.5590

TABLE II

COORDINATES OF TRANSITION SECTIONS FOR CONVEX BLADE PASSAGE $\gamma = 1.40$ - Concluded

$-\phi$	ν_e	$-X^*$	Y^*
$\nu_u = 28^\circ$			
18	10	0.3204	0.5543
19	9	.3349	.5495
20	8	.3489	.5445
21	7	.3622	.5395
22	6	.3746	.5347
$\nu_u = 26^\circ$			
0	26	0	0.6147
1	25	.0211	.6145
2	24	.0419	.6140
3	23	.0623	.6131
4	22	.0823	.6119
5	21	.1019	.6104
6	20	.1211	.6085
7	19	.1400	.6064
8	18	.1586	.6039
9	17	.1768	.6012
10	16	.1948	.5982
11	15	.2124	.5949
12	14	.2297	.5913
13	13	.2466	.5876
14	12	.2632	.5836
15	11	.2794	.5794
16	10	.2952	.5750
17	9	.3105	.5705
18	8	.3252	.5659
19	7	.3393	.5612
20	6	.3525	.5565
$\nu_u = 24^\circ$			
0	24	0	0.6277
1	23	.0215	.6275
2	22	.0428	.6270
3	21	.0636	.6261
4	20	.0840	.6248
5	19	.1040	.6232
6	18	.1237	.6213
7	17	.1430	.6191
8	16	.1619	.6167
9	15	.1806	.6139
10	14	.1988	.6108
11	13	.2167	.6075
12	12	.2342	.6040
$\nu_u = 24^\circ$			
13	11	0.2513	0.6002
14	10	.2680	.5962
15	9	.2842	.5920
16	8	.2998	.5877
17	7	.3147	.5832
18	6	.3288	.5788
$\nu_u = 22^\circ$			
0	22	0	0.6416
1	21	.0220	.6414
2	20	.0432	.6409
3	19	.0645	.6399
4	18	.0859	.6386
5	17	.1064	.6370
6	16	.1266	.6351
7	15	.1463	.6328
8	14	.1656	.6303
9	13	.1845	.6275
10	12	.2030	.6244
11	11	.2211	.6210
12	10	.2388	.6174
13	9	.2560	.6136
14	8	.2718	.6098
15	7	.2876	.6057
16	6	.3034	.6013
$\nu_u = 20^\circ$			
0	20	0	0.6566
1	19	.0226	.6564
2	18	.0448	.6558
3	17	.0666	.6549
4	16	.0880	.6536
5	15	.1089	.6519
6	14	.1295	.6499
7	13	.1496	.6477
8	12	.1692	.6451
9	11	.1885	.6422
10	10	.2072	.6391
11	9	.2255	.6357
12	8	.2431	.6321
13	7	.2601	.6284
14	6	.2761	.6245
$\nu_u = 18^\circ$			
0	18	0	0.6729
1	17	.0232	.6727
2	16	.0460	.6721
3	15	.0683	.6711
4	14	.0901	.6698
5	13	.1115	.6681
6	12	.1325	.6661
7	11	.1530	.6638
8	10	.1730	.6611
9	9	.1924	.6582
10	8	.2113	.6551
11	7	.2294	.6517
12	6	.2467	.6482
$\nu_u = 16^\circ$			
0	16	0	0.6907
1	15	.0242	.6905
2	14	.0471	.6899
3	13	.0700	.6889
4	12	.0923	.6875
5	11	.1142	.6858
6	10	.1356	.6838
7	9	.1564	.6814
8	8	.1766	.6788
9	7	.1961	.6758
10	6	.2147	.6727
$\nu_u = 12^\circ$			
0	12	0	0.7317
1	11	.0280	.7315
2	10	.0498	.7309
3	9	.0739	.7299
4	8	.0972	.7285
5	7	.1200	.7267
6	6	.1419	.7246
$\nu_u = 8^\circ$			
0	8	0	0.7833
1	7	.0269	.7831
2	6	.0531	.7824
$\nu_u = 4^\circ$			
0	4	0	0.8536
1	3	.0290	.8534
2	2	.0559	.8527

TABLE III

COORDINATES OF TRANSITION SECTIONS FOR CONCAVE BLADE PASSAGE $\gamma = 1.40$

$-\phi$	v_e	$-X^*$	Y^*
$v_1 = 0^\circ$			
0	0	0	1.0000
0.2	0.2	.0116	1.0000
0.4	0.4	.0192	.9999
0.6	0.6	.0260	.9999
0.8	0.8	.0347	.9998
1.0	1.0	.0607	.9992
2.0	2.0	.0953	.9983
3.0	3.0	.1302	.9967
4.0	4.0	.1741	.9965
5.0	5.0	.2184	.9930
6.0	6.0	.2632	.9862
7.0	7.0	.3086	.9810
8.0	8.0	.3546	.9750
9.0	9.0	.4015	.9680
10.0	10.0	.4491	.9850
11.0	11.0	.4915	.9522
12.0	12.0	.5409	.9420
13.0	13.0	.5975	.9295
14.0	14.0	.6494	.9171
15.0	15.0	.7025	.9033
16.0	16.0	.7571	.8882
17.0	17.0	.8132	.8716
18.0	18.0	.8707	.8534
19.0	19.0	.9299	.8336
20.0	20.0	.9909	.8120
21.0	21.0	1.0540	.7884
22.0	22.0	1.1192	.7627
23.0	23.0	1.1865	.7348
24.0	24.0	1.2560	.7046
25.0	25.0	1.3309	.6704
26.0	26.0	1.4059	.6346
27.0	27.0	1.4810	.5972
28.0	28.0	1.5617	.5552
29.0	29.0	1.6457	.5095
$v_1 = 1.0^\circ$			
0	1.0	0	0.9374
0.2	1.2	.00662	.9374
0.4	1.4	.01343	.9374
0.6	1.6	.02036	.9373
0.8	1.8	.02738	.9373
1.0	2.0	.04165	.9370
2.0	3.0	.07091	.9362
3.0	4.0	.1084	.9346
4.0	5.0	.1467	.9322
5.0	6.0	.1857	.9291
6.0	7.0	.2254	.9253
7.0	8.0	.2659	.9207
8.0	9.0	.3070	.9153
9.0	10.0	.3489	.9090
10.0	11.0	.3918	.9019
11.0	12.0	.4355	.8938
12.0	13.0	.4800	.8847
13.0	14.0	.5257	.8746
14.0	15.0	.5725	.8633
15.0	16.0	.6204	.8509
16.0	17.0	.6697	.8373
17.0	18.0	.7203	.8223
18.0	19.0	.7233	.8059
19.0	20.0	.8259	.7880
20.0	21.0	.8810	.7684
21.0	22.0	.9381	.7471
22.0	23.0	.9969	.7239
23.0	24.0	1.0578	.6987
24.0	25.0	1.1208	.6713
25.0	26.0	1.1860	.6416
26.0	27.0	1.2288	.6093
27.0	28.0	1.3241	.5742
28.0	29.0	1.3970	.5362
$v_1 = 2^\circ$			
0	2	0	0.9035
1	3	.0326	.9032
2	4	.0667	.9023
3	5	.1018	.9008
4	6	.1377	.8986
5	7	.1743	.8957
6	8	.2118	.8921
7	9	.2499	.8878
8	10	.2888	.8826
9	11	.3285	.8767
10	12	.3690	.8699
11	13	.4104	.8622
12	14	.4528	.8536
13	15	.4962	.8440
14	16	.5407	.8333
15	17	.5863	.8215
16	18	.6332	.8085
17	19	.6814	.7942
18	20	.7279	.7795
19	21	.7788	.7624
20	22	.8344	.7428
21	23	.8888	.7224
22	24	.9450	.7003
23	25	1.0031	.6762
24	26	1.0632	.6501
25	27	1.1256	.6216
26	28	1.1904	.5907
27	29	1.2576	.5571
$v_1 = 4^\circ$			
0	4	0	0.8536
1	5	.0305	.8533
2	6	.0619	.8525
3	7	.0941	.8511
4	8	.1272	.8491
5	9	.1610	.8464
6	10	.1954	.8431
7	11	.2306	.8391
8	12	.2666	.8344
9	13	.3033	.8289
10	14	.3407	.8226
11	15	.3792	.8154
12	16	.4188	.8074
13	17	.4593	.7984
14	18	.5008	.7884
15	19	.5434	.7774
16	20	.5872	.7653
17	21	.6323	.7519
18	22	.6788	.7372
19	23	.7267	.7212
20	24	.7761	.7037
21	25	.8272	.6846
22	26	.8802	.6637
23	27	.9350	.6410
24	28	.9918	.6163
25	29	1.0507	.5894
$v_1 = 6^\circ$			
0	6	0	0.8152
1	7	.0290	.8150
2	8	.0587	.8142
3	9	.0891	.8129
4	10	.1203	.8110
5	11	.1522	.8084
6	12	.1847	.8053
7	13	.2178	.8015
8	14	.2518	.7970
9	15	.2866	.7918
10	16	0.3223	0.7859
11	17	.3588	.7791
12	18	.3962	.7715
13	19	.4346	.7630
14	20	.4740	.7535
15	21	.5146	.7430
16	22	.5564	.7314
17	23	.5994	.7186
18	24	.6438	.7046
19	25	.6897	.6893
20	26	.7371	.6725
21	27	.7861	.6541
22	28	.8369	.6341
23	29	.8896	.6123
$v_1 = 8^\circ$			
0	8	0	0.7833
1	9	.0278	.7831
2	10	.0562	.7823
3	11	.0853	.7810
4	12	.1150	.7792
5	13	.1453	.7768
6	14	.1764	.7739
7	15	.2081	.7702
8	16	.2406	.7659
9	17	.2739	.7610
10	18	.3080	.7553
11	19	.3430	.7488
12	20	.3788	.7415
13	21	.4157	.7333
14	22	.4537	.7242
15	23	.4927	.7141
16	24	.5331	.7029
17	25	.5746	.6906
18	26	.6173	.6771
19	27	.6617	.6622
20	28	.7076	.6460
21	29	.7552	.6282
$v_1 = 10^\circ$			
0	10	0	0.7559
1	11	.0269	.7557
2	12	.0542	.7550
3	13	.0821	.7537
4	14	.1106	.7520
5	15	.1399	.7497
6	16	.1698	.7468
7	17	.2004	.7433
8	18	.2316	.7392
9	19	.2667	.7344
10	20	.2972	.7288
11	21	.3310	.7225
12	22	.3651	.7156
13	23	.4007	.7077
14	24	.4374	.6989
15	25	.4774	.6885
16	26	.5165	.6777
17	27	.5550	.6663
18	28	.5967	.6531
19	29	.6399	.6386
20	30	.6846	.6228
21	31	.7311	.6054
22	32	.7794	.5864
23	33	.8296	.5656
24	34	.8820	.5428
25	35	.9365	.5179
26	36	.9934	.4908
27	37	1.0529	.4611
28	38	1.1152	.4286

NACA

TABLE III

COORDINATES OF TRANSITION SECTIONS FOR CONCAVE BLADE PASSAGE $\gamma = 1.40$ - Concluded

$-\phi$	ν_e	$-X^*$	Y^*
	$\nu_1 = 12^\circ$		
0	12	0	0.7317
1	13	.0259	.7315
2	14	.0523	.7308
3	15	.0793	.7296
4	16	.1069	.7279
5	17	.1351	.7257
6	18	.1640	.7229
7	19	.1936	.7195
8	20	.2238	.7156
9	21	.2549	.7109
10	22	.2868	.7056
11	23	.3195	.6995
12	24	.3532	.6926
13	25	.3879	.6849
14	26	.4237	.6763
15	27	.4606	.6668
16	28	.4987	.6562
17	29	.5381	.6445
18	30	.5789	.6317
19	31	.6212	.6175
20	32	.6651	.6020
21	33	.7108	.5849
22	34	.7583	.5661
23	35	.8077	.5457
24	36	.8592	.5232
25	37	.9132	.4986
26	38	.9697	.4717
	$\nu_1 = 14^\circ$		
0	14	0	0.7102
1	15	.0252	.7100
2	16	.0509	.7093
3	17	.0771	.7082
4	18	.1038	.7065
5	19	.1312	.7044
6	20	.1592	.7017
7	21	.1879	.6984
8	22	.2174	.6945
9	23	.2476	.6900
10	24	.2787	.6848
11	25	.3106	.6789
12	26	.3435	.6722
13	27	.3774	.6647
14	28	.4124	.6563
15	29	.4485	.6469
16	30	.4858	.6365
17	31	.5245	.6251
18	32	.5648	.6124
19	33	.6065	.5984
20	34	.6496	.5831
21	35	.6946	.5663
22	36	.7415	.5478
23	37	.7906	.5275
24	38	.8419	.5051
	$\nu_1 = 16^\circ$		
0	16	0	0.6907
1	17	.0246	.6905
2	18	.0495	.6898
3	19	.0749	.6887
4	20	.1009	.6871
5	21	.1276	.6850
6	22	0.1549	0.6824
7	23	.1829	.6792
8	24	.2116	.6754
9	25	.2411	.6710
10	26	.2714	.6659
11	27	.3027	.6601
12	28	.3349	.6536
13	29	.3681	.6462
14	30	.4023	.6380
15	31	.4378	.6288
16	32	.4746	.6186
17	33	.5127	.6073
18	34	.5522	.5948
19	35	.5933	.5811
20	36	.6361	.5659
21	37	.6809	.5492
22	38	.7275	.5308
	$\nu_1 = 18^\circ$		
0	18	0	0.6729
1	19	.0239	.6727
2	20	.0481	.6721
3	21	.0729	.6710
4	22	.0984	.6694
5	23	.1243	.6674
6	24	.1509	.6648
7	25	.1783	.6617
8	26	.2064	.6580
9	27	.2352	.6537
10	28	.2649	.6487
11	29	.2955	.6430
12	30	.3271	.6366
13	31	.3597	.6294
14	32	.3934	.6213
15	33	.4284	.6122
16	34	.4647	.6021
17	35	.5022	.5910
18	36	.5414	.5786
19	37	.5822	.5650
20	38	.6247	.5499
21	39	.6682	.5337
	$\nu_1 = 20^\circ$		
0	20	0	0.6566
1	21	.0233	.6564
2	22	.0470	.6558
3	23	.0712	.6547
4	24	.0960	.6532
5	25	.1214	.6512
6	26	.1475	.6487
7	27	.1743	.6456
8	28	.2017	.6420
9	29	.2300	.6378
10	30	.2591	.6329
11	31	.2892	.6273
12	32	.3203	.6210
13	33	.3525	.6139
14	34	.3858	.6059
15	35	.4202	.5970
16	36	.4560	.5870
17	37	.4933	.5760
18	38	.5322	.5637
	$\nu_1 = 22^\circ$		
0	22	0	0.6416
1	23	.0228	.6414
2	24	.0459	.6408
3	25	.0697	.6398
4	26	.0939	.6383
5	27	.1188	.6363
6	28	.1444	.6339
7	29	.1706	.6309
8	30	.1976	.6273
9	31	.2254	.6232
10	32	.2541	.6183
11	33	.2838	.6128
12	34	.3144	.6066
13	35	.3460	.5996
14	36	.3789	.5917
15	37	.4132	.5828
16	38	.4488	.5729
	$\nu_1 = 26^\circ$		
0	26	0	0.6147
1	27	.0218	.6145
2	28	.0441	.6139
3	29	.0668	.6130
4	30	.0901	.6115
5	31	.1141	.6096
6	32	.1388	.6073
7	33	.1642	.6044
8	34	.1903	.6009
9	35	.2172	.5969
10	36	.2451	.5922
11	37	.2741	.5868
12	38	.3041	.5807
	$\nu_1 = 30^\circ$		
0	30	0	0.5913
1	31	.0210	.5911
2	32	.0423	.5905
3	33	.0642	.5895
4	34	.0868	.5881
5	35	.1098	.5863
6	36	.1337	.5840
7	37	.1584	.5812
8	38	.1839	.5778
9	39	.2094	.5740
	$\nu_1 = 34^\circ$		
0	34	0	0.5707
1	35	.0202	.5705
2	36	.0409	.5700
3	37	.0622	.5691
4	38	.0842	.5677
5	39	.1058	.5660
	$\nu_1 = 36^\circ$		
0	36	0	0.5614
1	37	.0212	.5612
2	38	.0418	.5607

NACA

TABLE IV

WEIGHTED AVERAGE PRESSURE RECOVERIES (PERCENTAGE)

(a) Blade I

Source	Pressure recovery
Entire span	88.0
1.20 inches from wall	89.3
1.00 inches from wall	94.9
0.80 inches from wall	90.6
0.60 inches from wall	85.0
0.40 inches from wall	81.4
0.20 inches from wall	84.6

(b) Blade II

Source	Pressure recovery
Entire span	87.6
1.13 inches from wall	84.8
0.93 inches from wall	90.5
0.73 inches from wall	89.5
0.53 inches from wall	81.3
0.33 inches from wall	87.4
0.13 inches from wall	90.1

(c) Blade III

Source	Pressure recovery
Entire span	87.8
1.13 inches from wall	85.8
0.93 inches from wall	85.6
0.73 inches from wall	84.6
0.53 inches from wall	87.1
0.33 inches from wall	90.8
0.13 inches from wall	91.0

(d) Blade IV

Source	Pressure recovery
Entire span	86.9
1.20 inches from wall	88.7
1.00 inches from wall	88.6
0.80 inches from wall	81.8
0.60 inches from wall	83.2
0.40 inches from wall	92.0
0.20 inches from wall	85.3

NACA

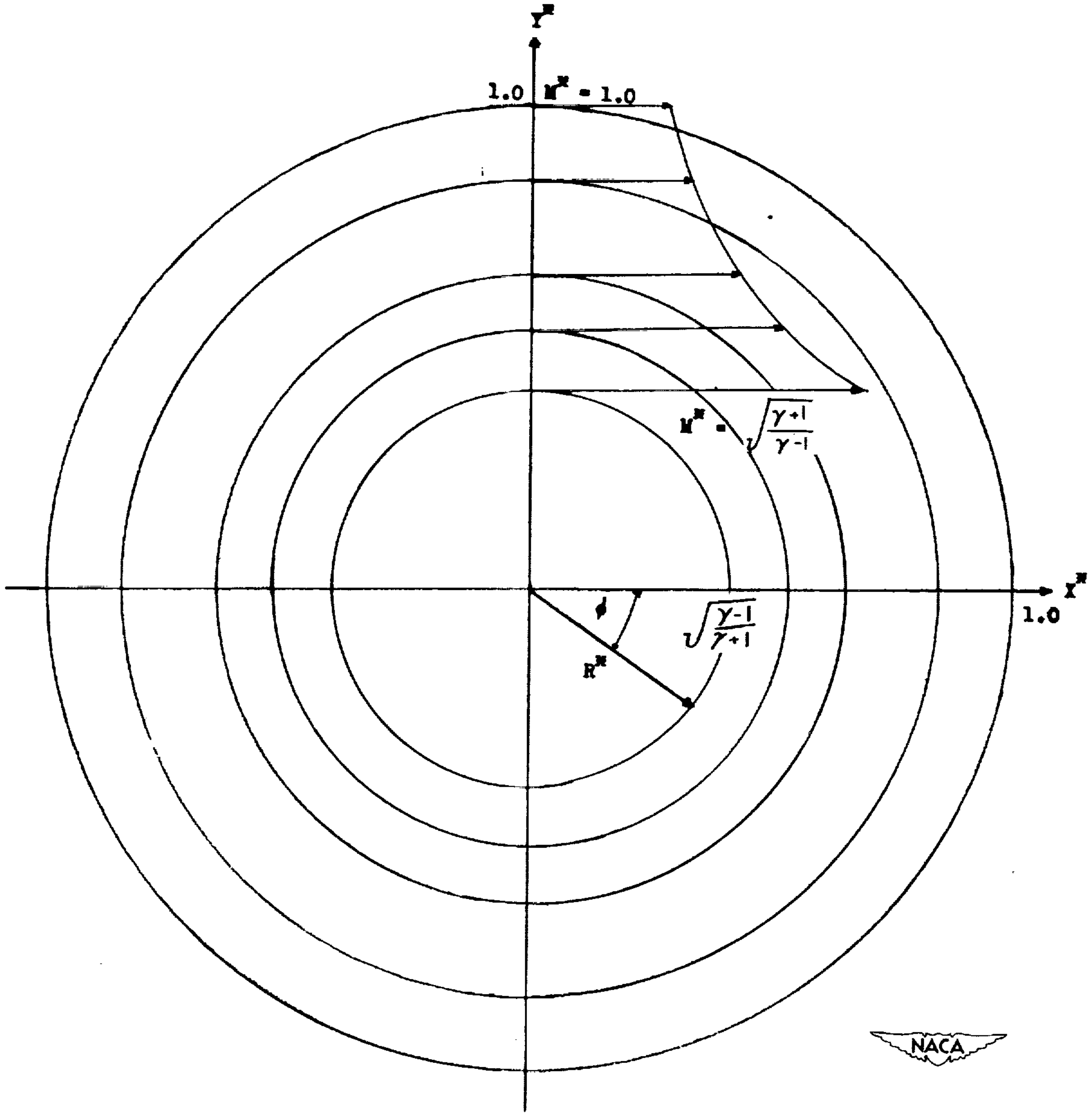
Y^*
1.0
$M^* = 1.0$
$M^* = \sqrt{\frac{\gamma+1}{\gamma-1}}$
X^*
1.0
ϕ
R^*
$\sqrt{\frac{\gamma-1}{\gamma+1}}$
NACA

Figure 1.- Supersonic realm of vortex flow.

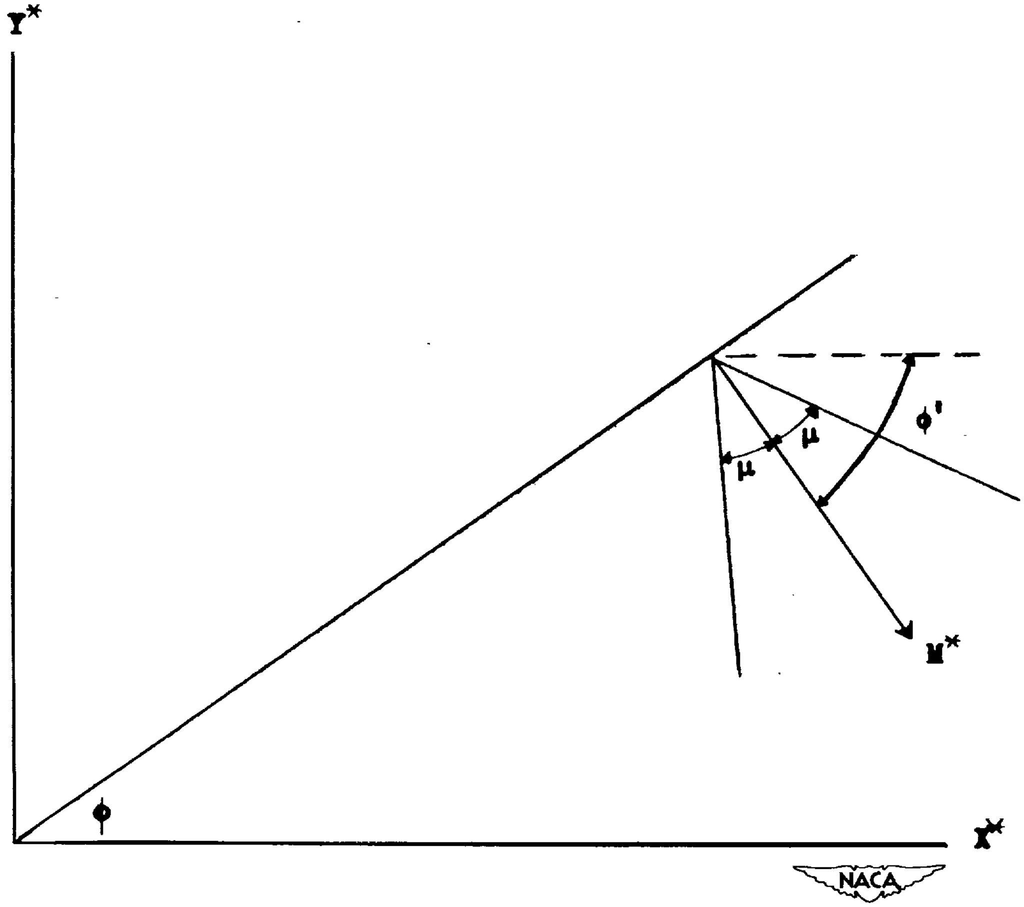
Y^*
X^*
ϕ
ϕ'
μ
μ
M^*
NACA

Figure 2.- Geometry of vortex field.

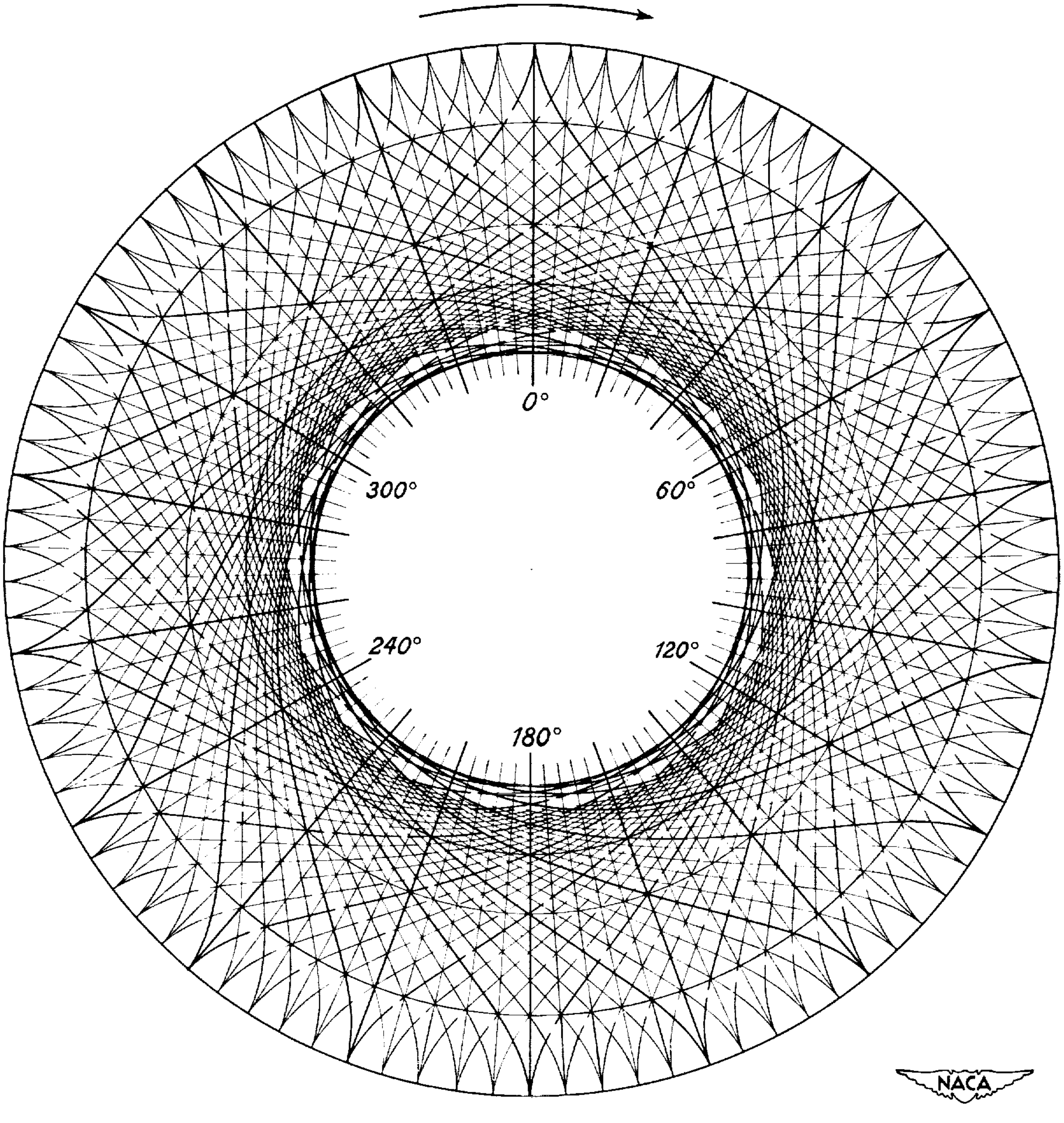
0°
60°
120°
180°
240°
300°
NACA

Figure 3.- Characteristic line network for supersonic vortex flow according to A. Busemann. $\gamma = 1.40$.

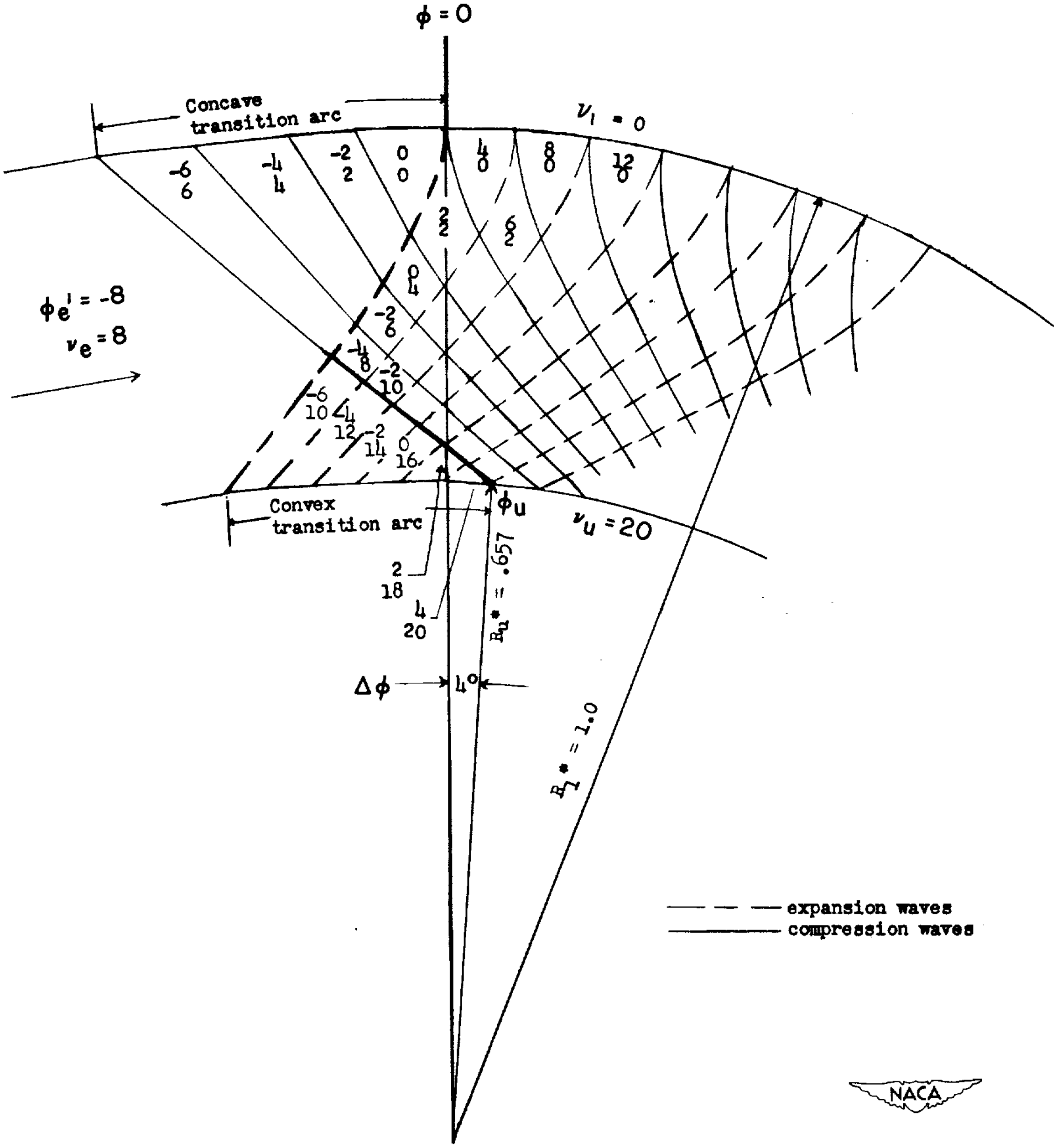
$\phi = 0$
Concave transition arc
$\nu_l = 0$
-6 6
-4 4
-2 2
0 0
4 0
8 0
12 0
2 2
6 2
0 4
-2 6
-4 8
-2 10
-6 10
-4 12
-2 14
0 16
$\phi_e' = -8$
$\nu_e = 8$
Convex transition arc
ϕ_u
$\nu_u = 20$
2 18
4 20
$R_u^* = .657$
$\Delta\phi$
4°
$R_l^* = 1.0$
expansion waves
compression waves

Figure 4.- Construction of transition arcs.

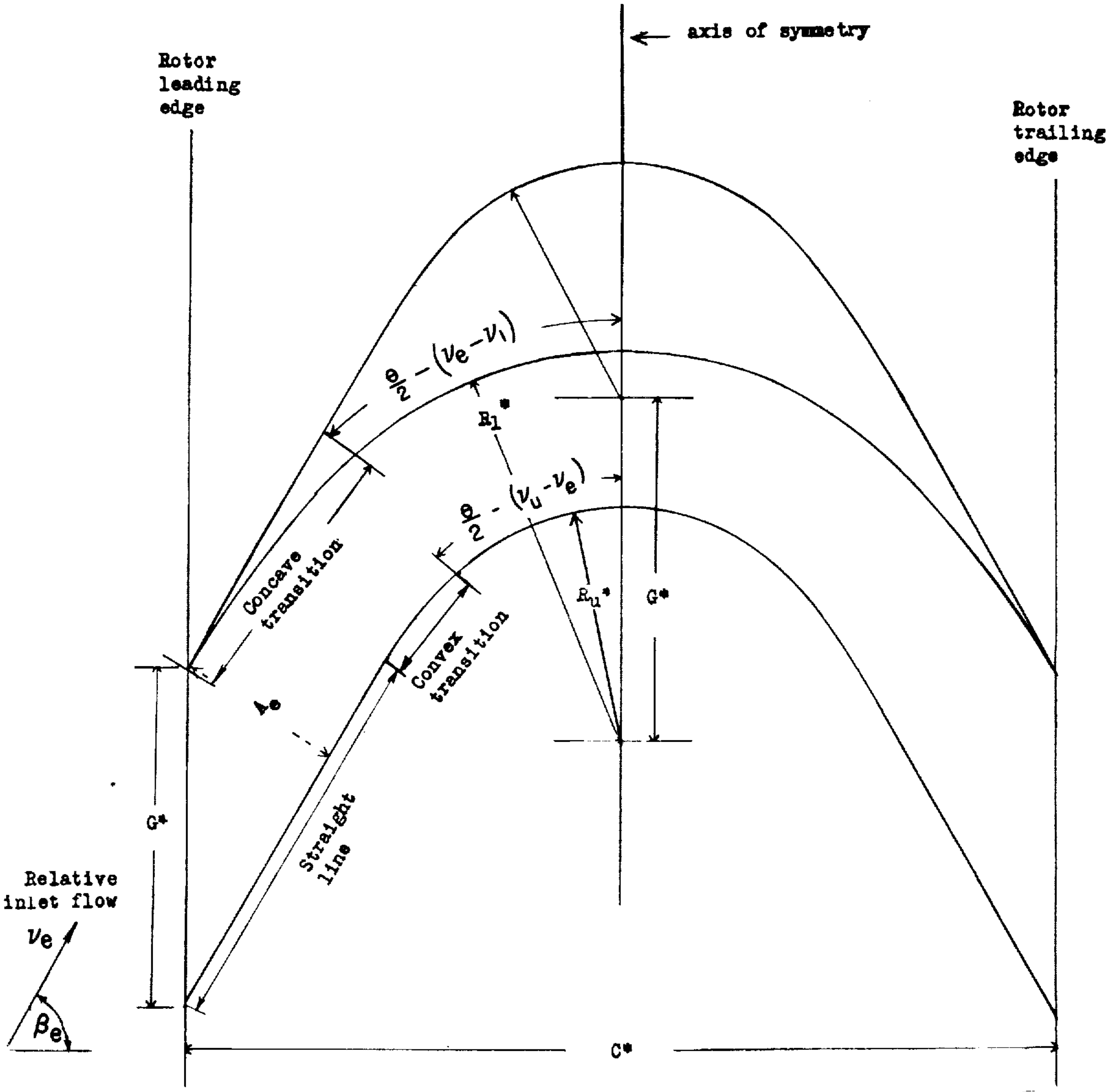
axis of symmetry
Rotor leading edge
Rotor trailing edge
$\frac{\theta}{2} - (\nu_e - \nu_1)$
R_1^*
$\frac{\theta}{2} - (\nu_u - \nu_e)$
Concave transition
Convex transition
R_u^*
G*
λ_e
Straight line
G*
Relative inlet flow
ν_e
β_e
C*

Figure 5.- Construction of typical symmetrical blade section.

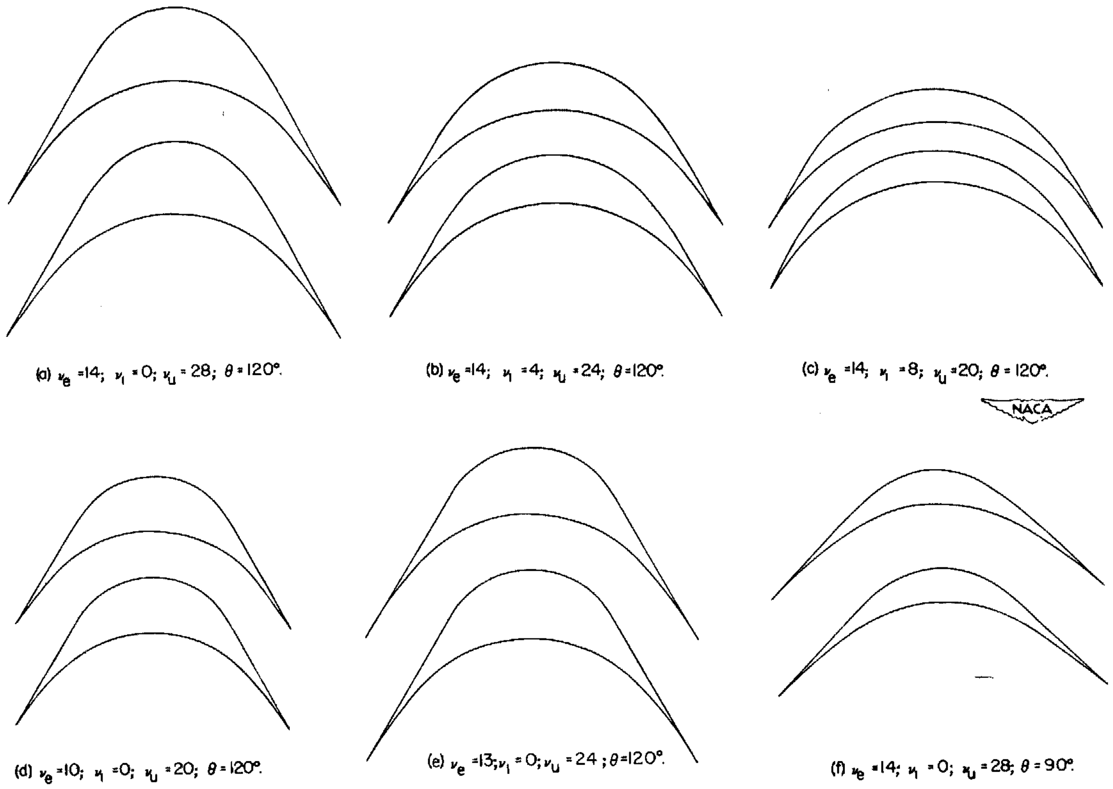

(a) $\nu_e = 14$; $\nu_l = 0$; $\nu_u = 28$; $\theta = 120^\circ$.

(b) $\nu_e = 14$; $\nu_l = 4$; $\nu_u = 24$; $\theta = 120^\circ$.

(c) $\nu_e = 14$; $\nu_l = 8$; $\nu_u = 20$; $\theta = 120^\circ$.

(d) $\nu_e = 10$; $\nu_l = 0$; $\nu_u = 20$; $\theta = 120^\circ$.

(e) $\nu_e = 13$; $\nu_l = 0$; $\nu_u = 24$; $\theta = 120^\circ$.

(f) $\nu_e = 14$; $\nu_l = 0$; $\nu_u = 28$; $\theta = 90^\circ$.

Figure 6.- Examples of blades.

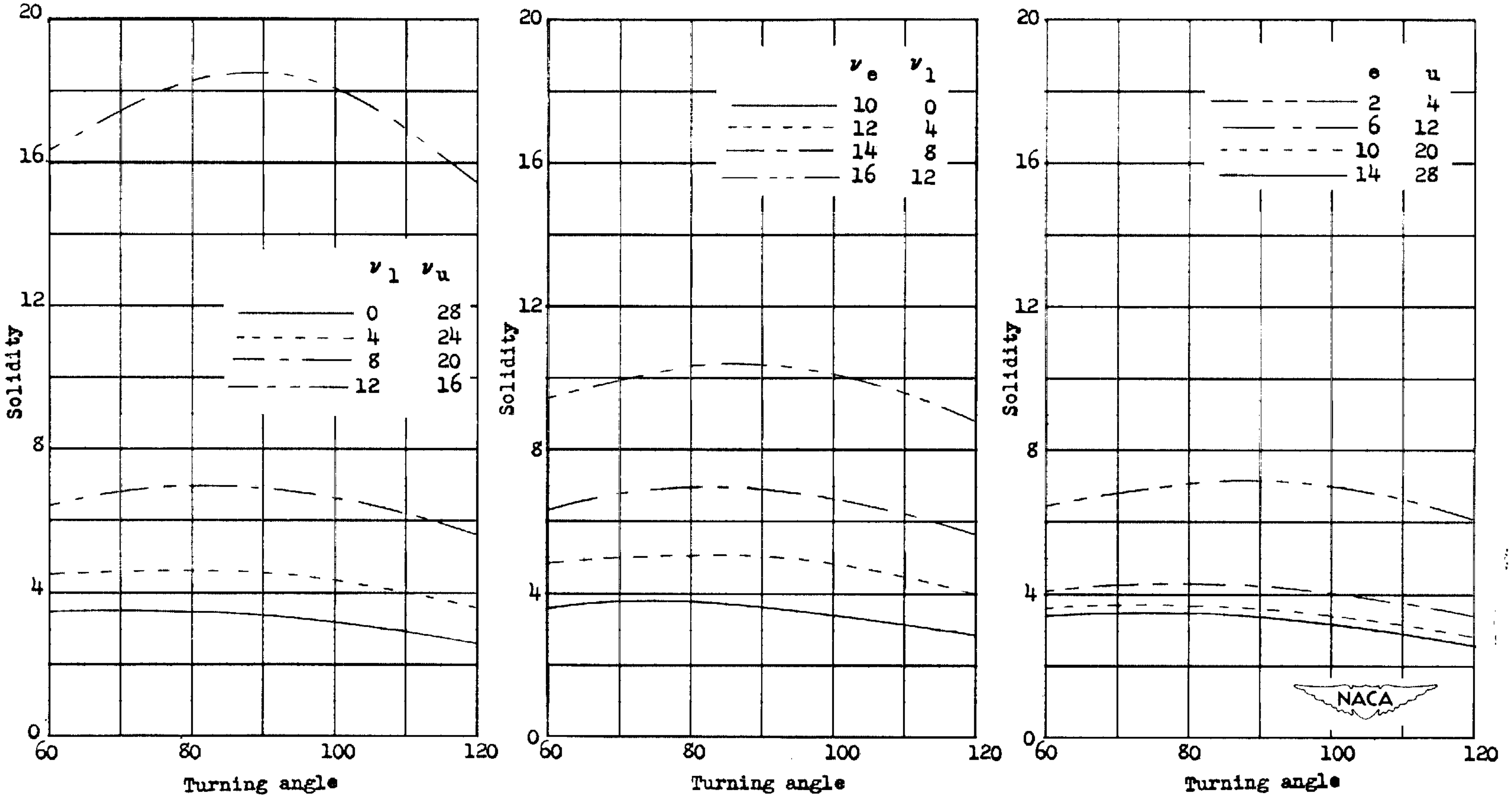

(a) $\nu_e = 14$.

(b) $\nu_u = 20$.

(c) $\nu_1 = 0$.

Figure 7.- Variation of solidity with turning angle for special case where $\nu_e = \frac{1}{2}(\nu_u + \nu_1)$.

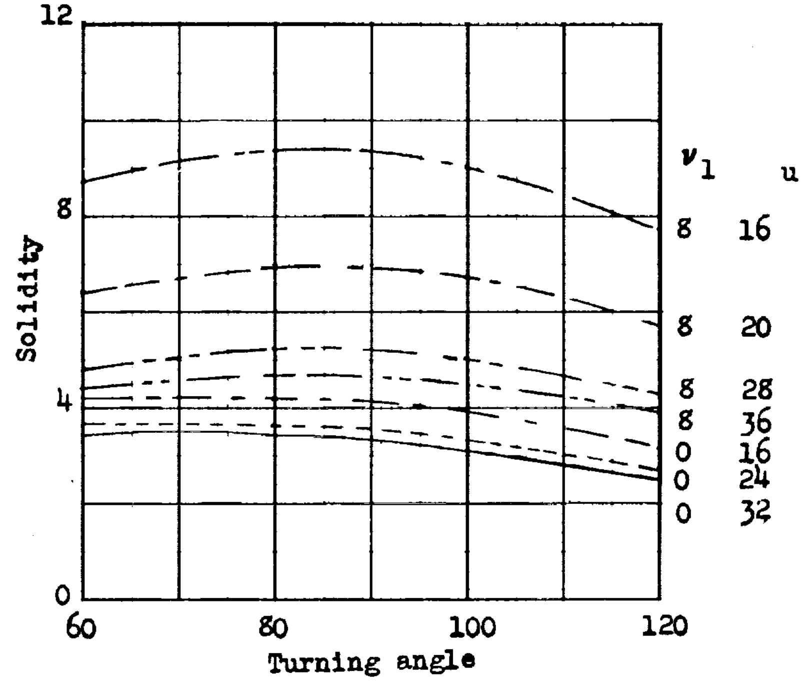

(a) $\nu_e = 14$.

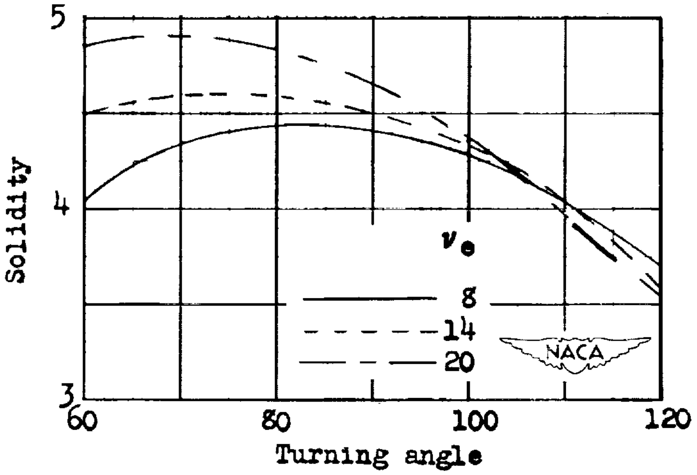

(b) $\nu_u = 24$ and $\nu_1 = 4$.

Figure 8.- Variation of solidity with turning angle for general case.

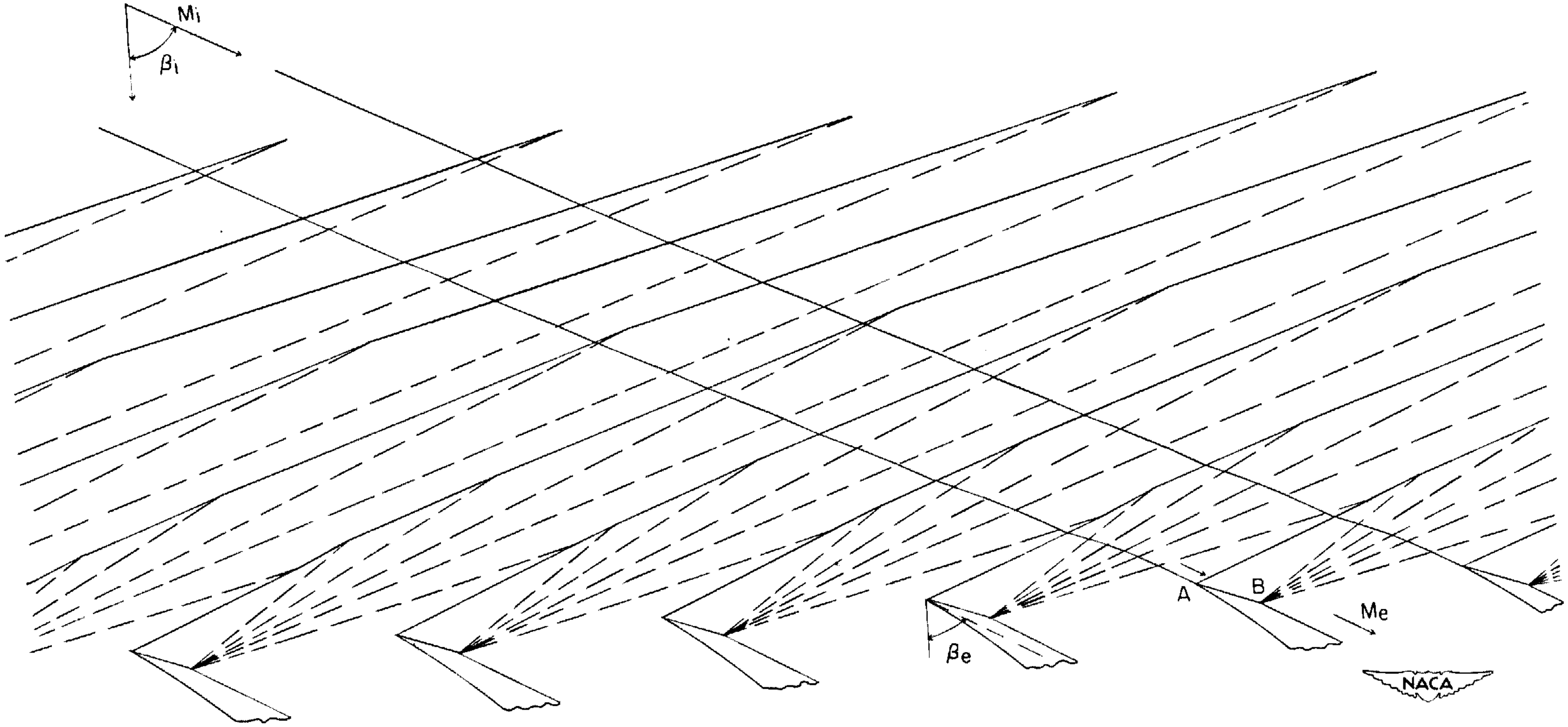
M_i
β_i
A
B
M_e
β_e
NACA

(a) Subsonic axial velocity component, external waves.

Figure 9.- Methods of increasing section thickness.

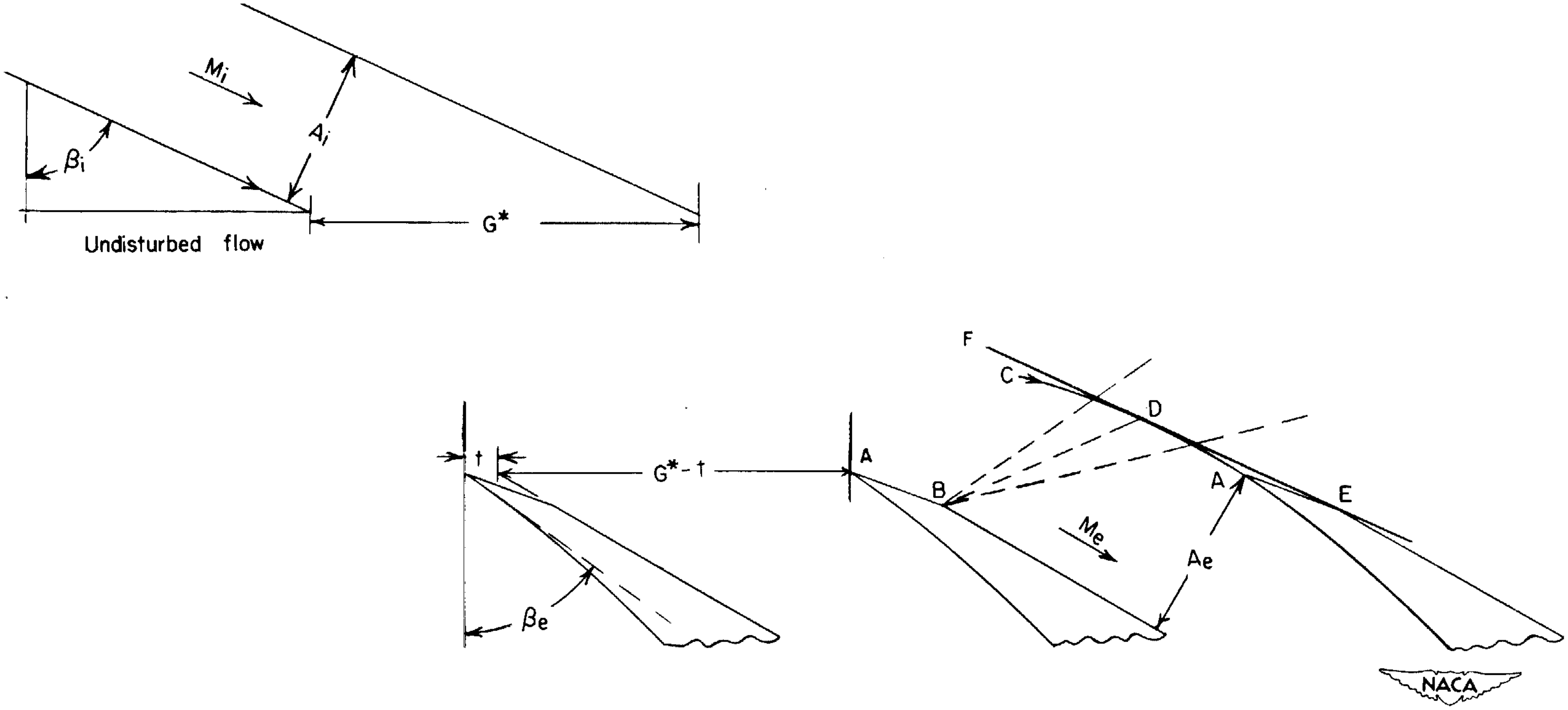
M_i
A_i
β_i
Undisturbed flow
G*
t
G*- t
A
B
C
D
E
F
A
M_e
A_e
β_e

(b) Flow geometry for external waves.

Figure 9.- Continued.

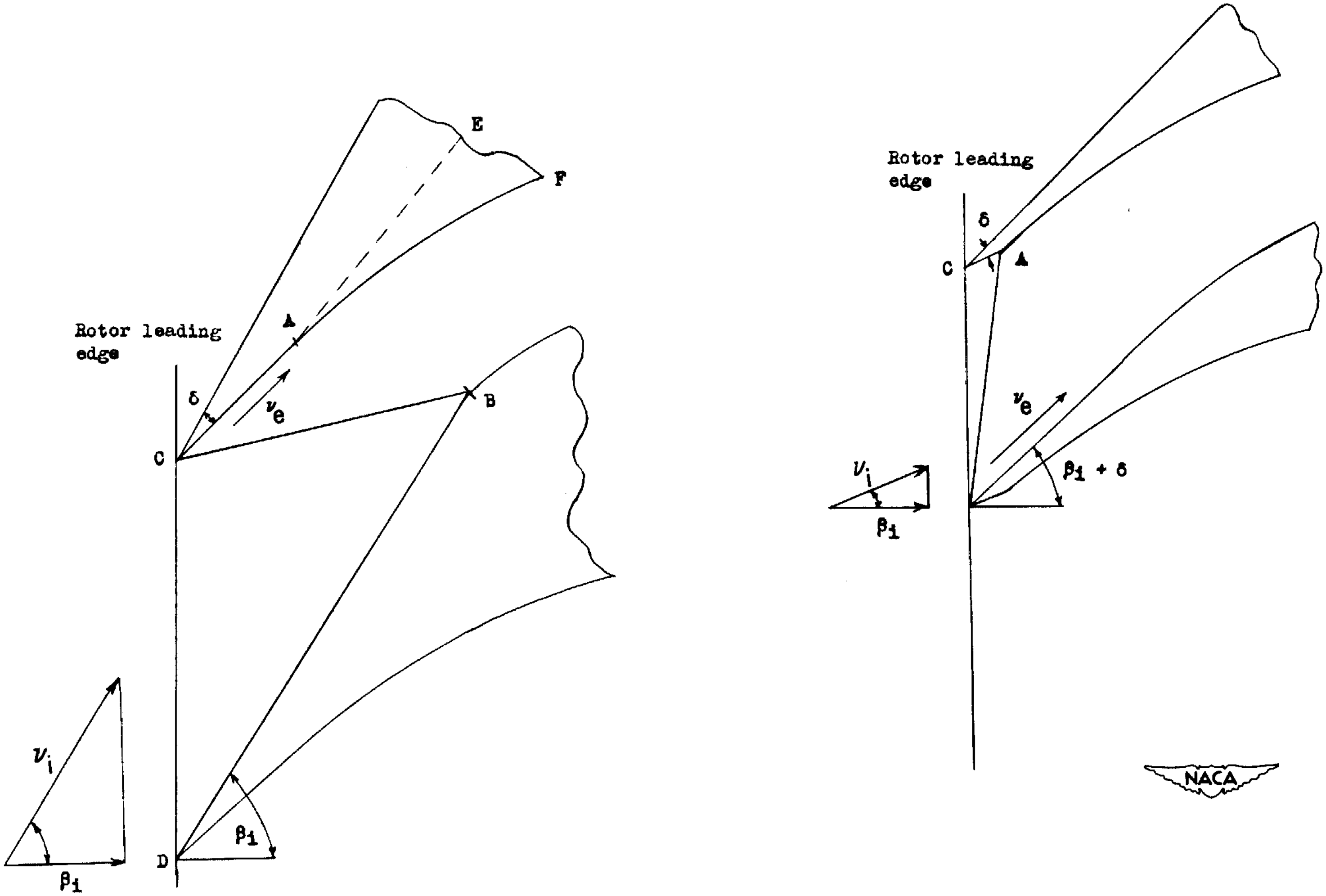
E
F
A
Rotor leading edge
δ
ν_e
B
C
ν_i
β_i
D
β_i
Rotor leading edge
δ
C
A
ν_e
ν_i
$\beta_i + \delta$
β_i

(c) Subsonic axial-velocity-component shock originating on concave surface.

(d) Supersonic axial-velocity component.

Figure 9.- Concluded.

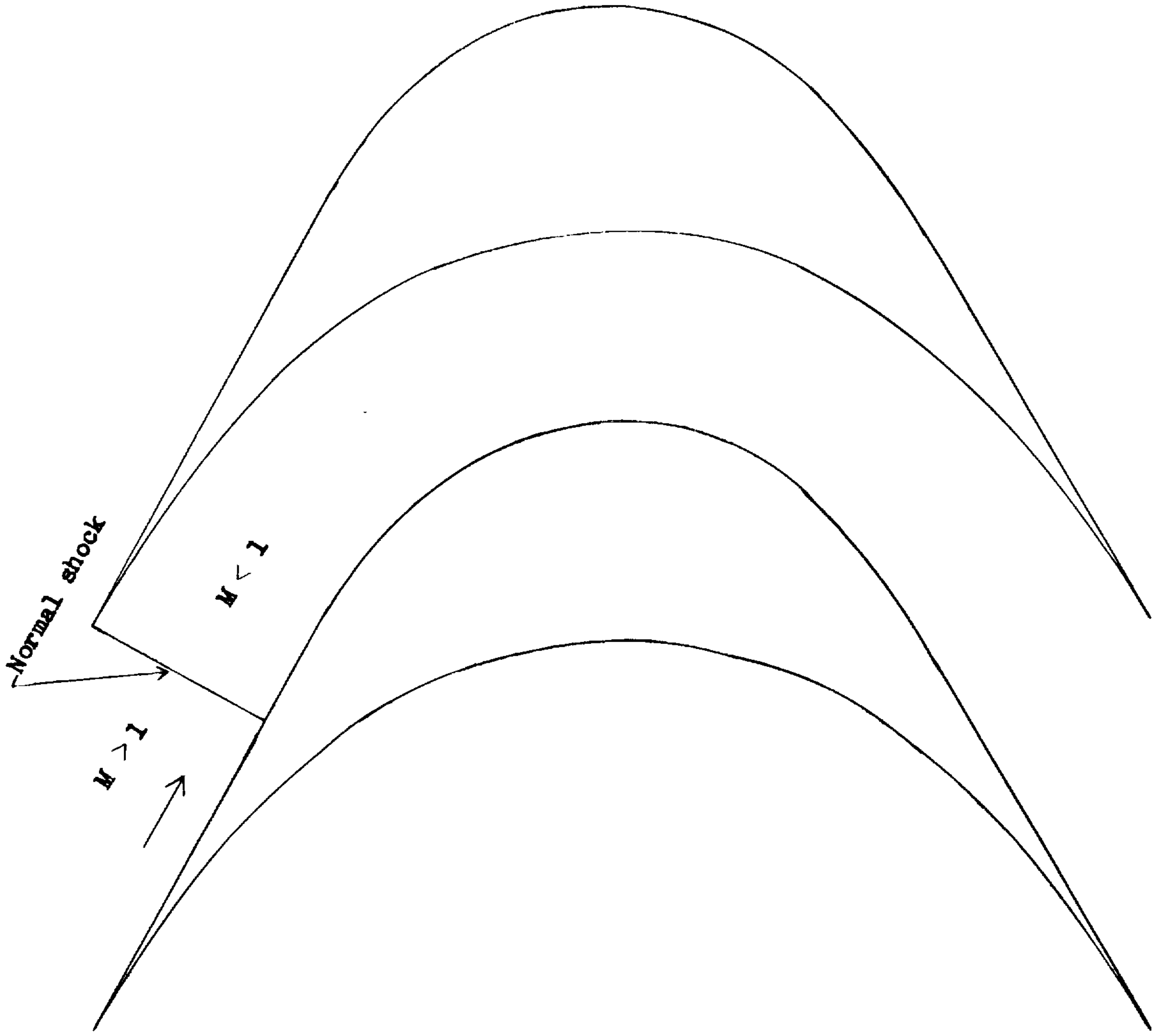
Normal shock
M < 1
M > 1

Figure 10.- Diagram of flow in the channel at the instant immediately before starting.

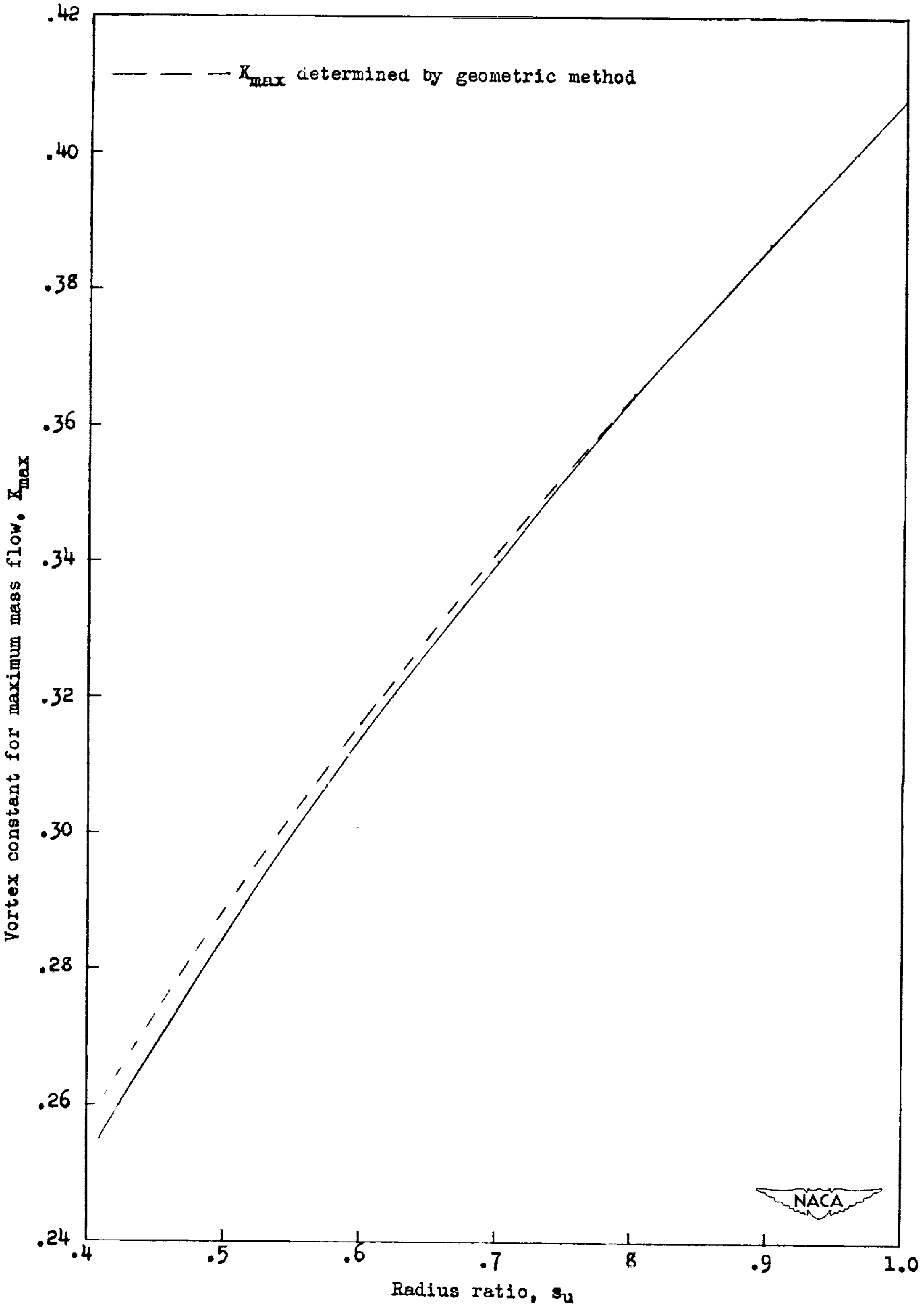

Figure 11.- Value of K_{max} as function of radius ratio for $\gamma = 1.40$.

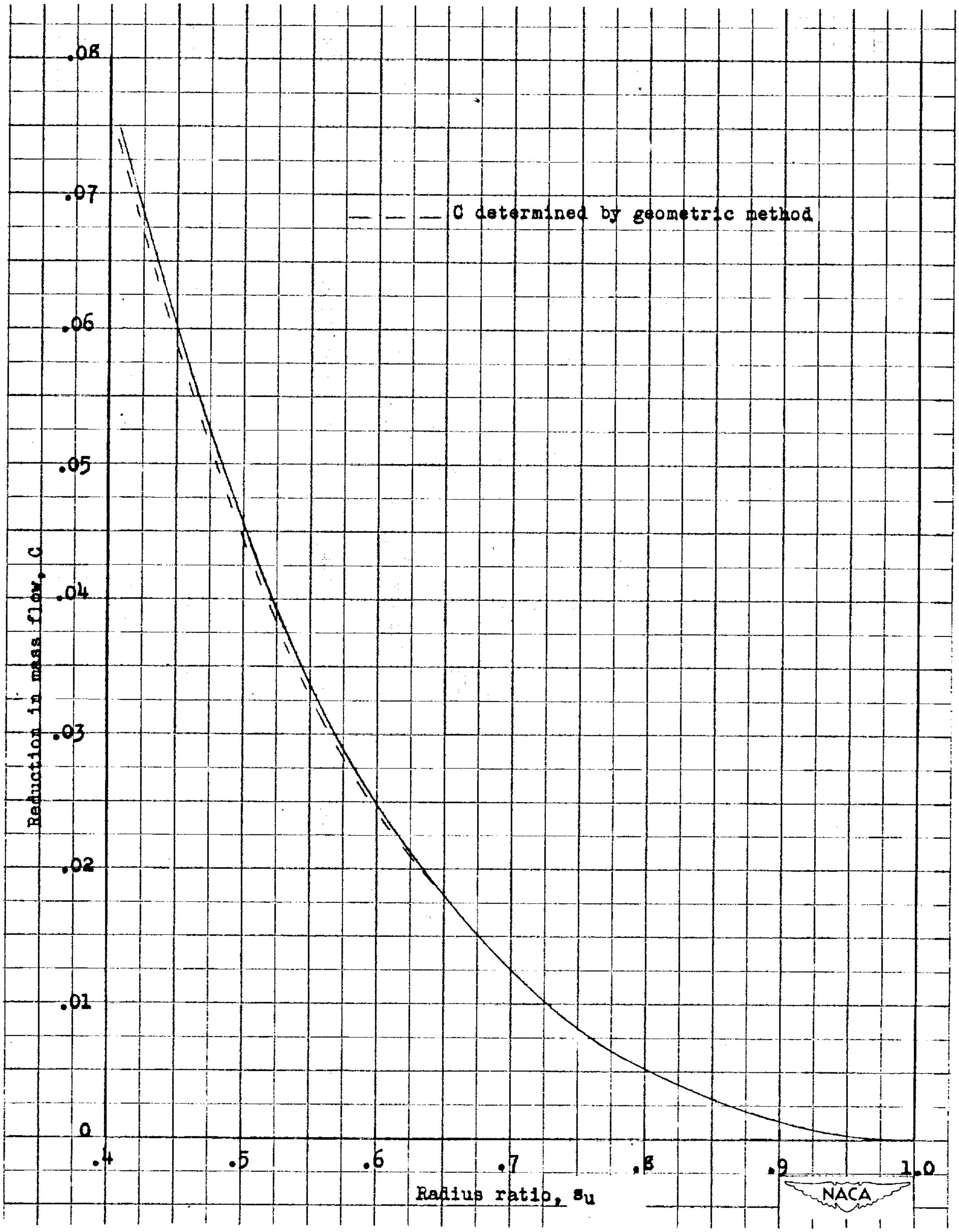

Figure 12.- Reduction in maximum mass flow as function of radius ratio for $\gamma = 1.40$.

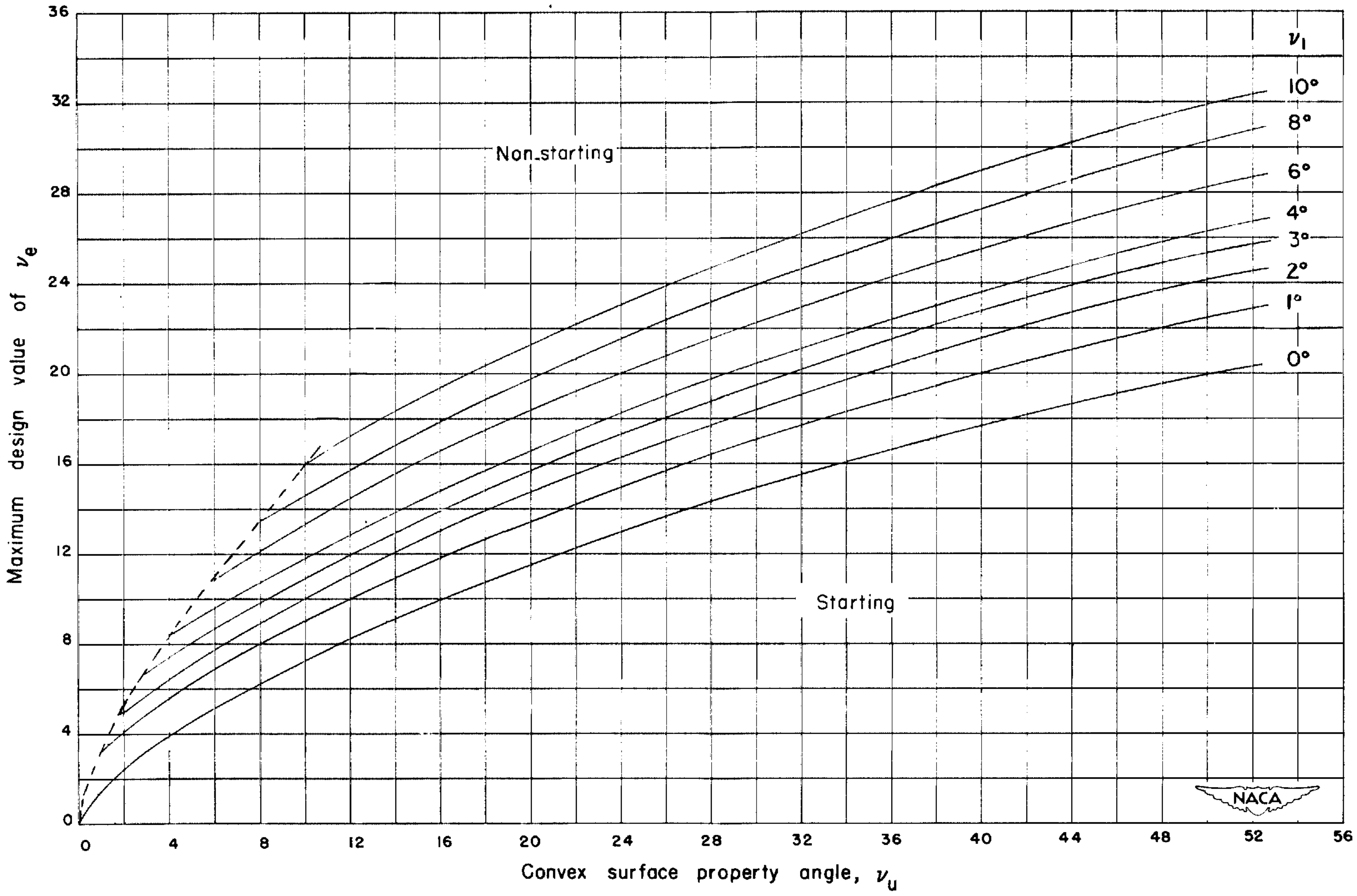

Figure 13.- Maximum design-inlet value of ν_e for starting as a function of ν_1 and ν_u.

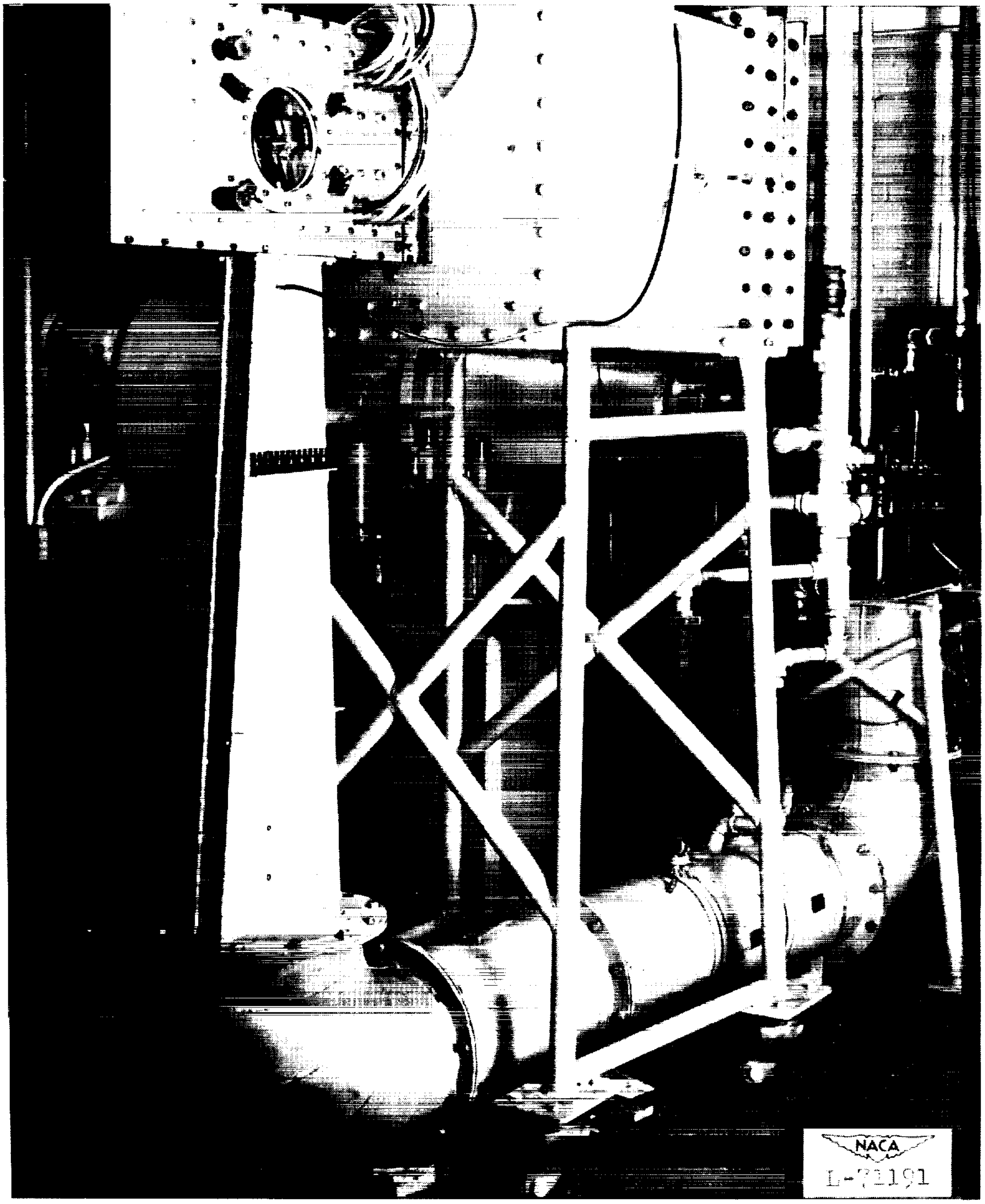

Figure 14.- Photo of $2\frac{1}{4}$- by 2-inch supersonic cascade tunnel.

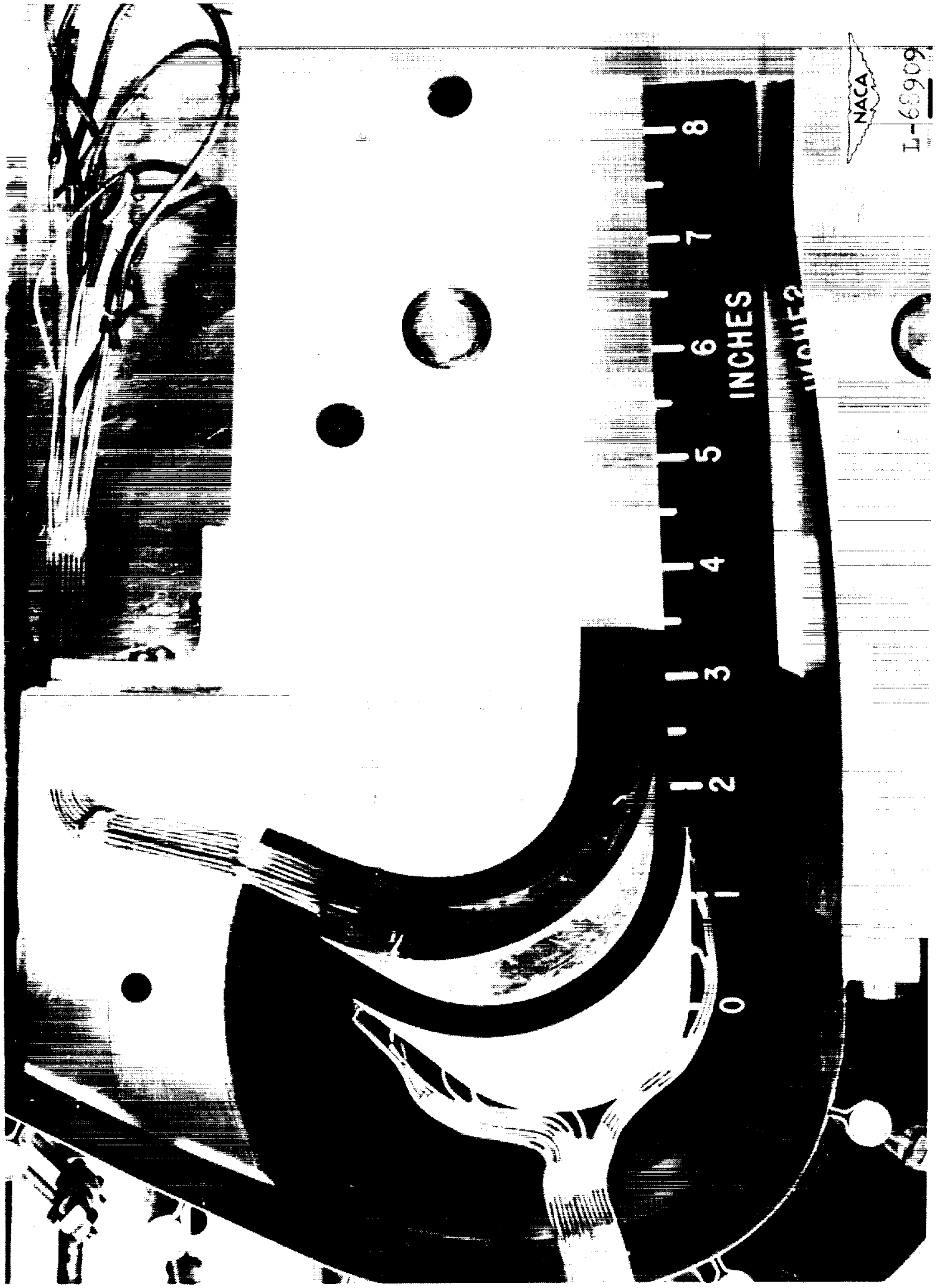
INCHES
0
1
2
3
4
5
6
7
8
NACA
L-68909

Figure 15.- View of test section with one side wall removed.

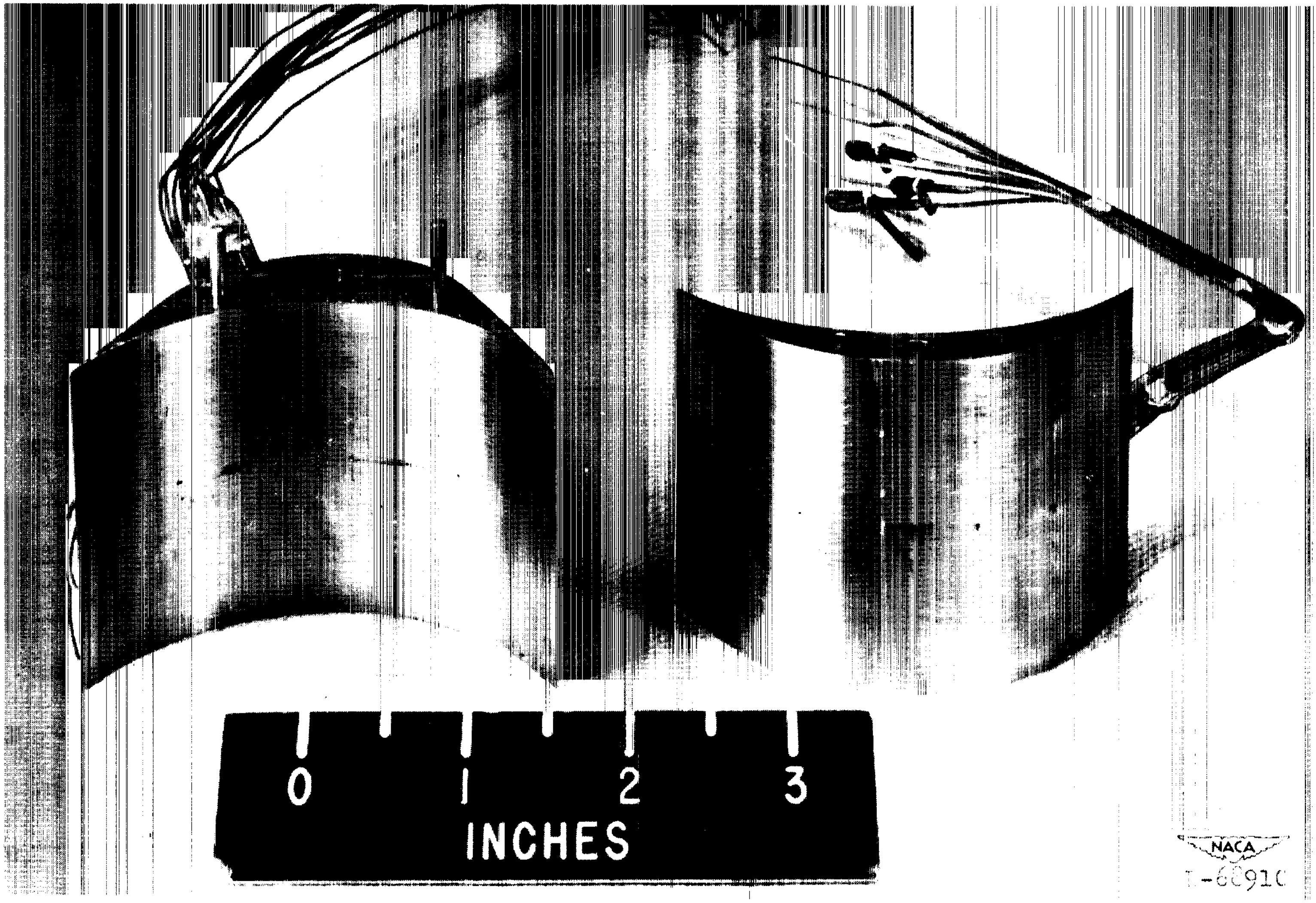
0
1
2
3
INCHES
NACA
L-68910

Figure 16.- Close up of blade I showing the static-pressure orifices and scratches.

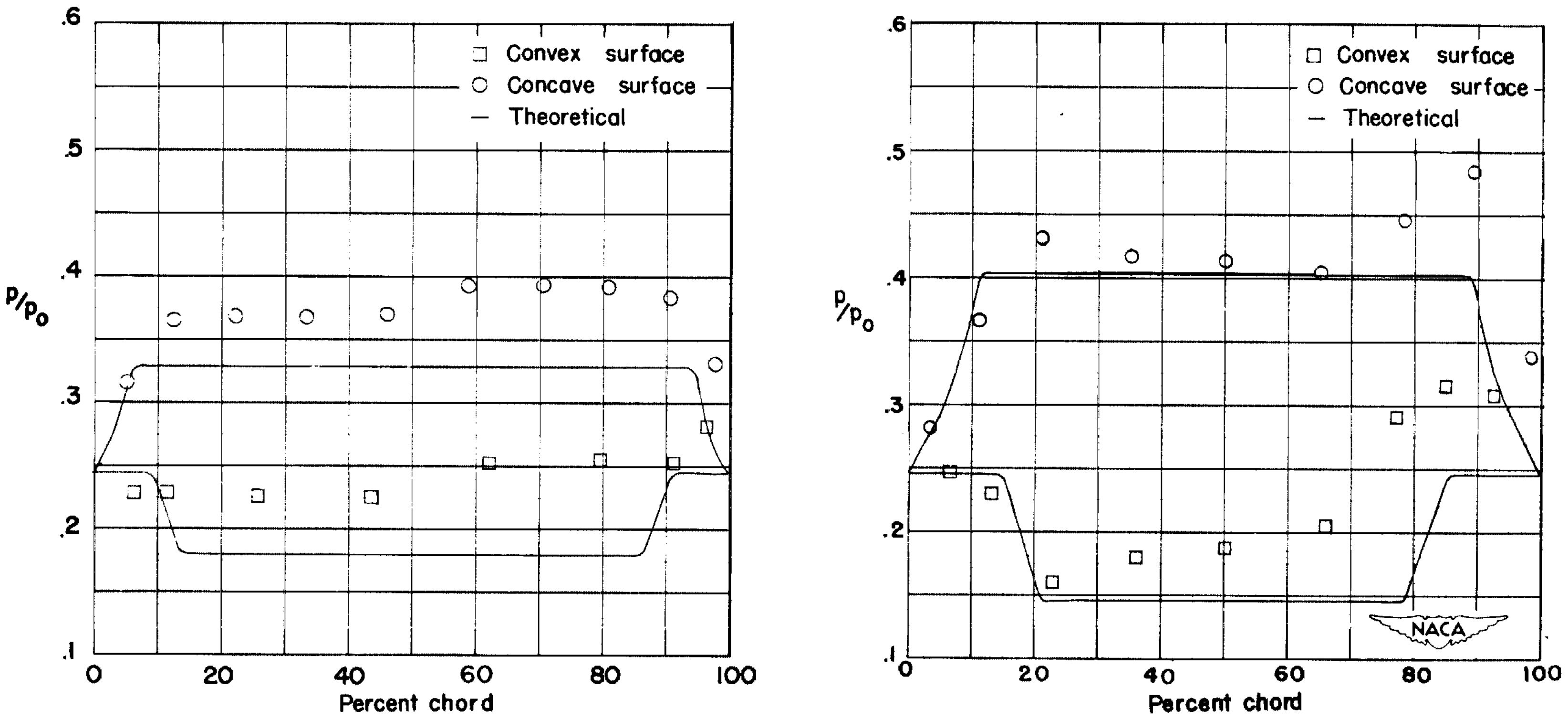

(a) Blade I.

(b) Blade II.

Figure 17.- Pressure distribution along concave and convex surfaces.

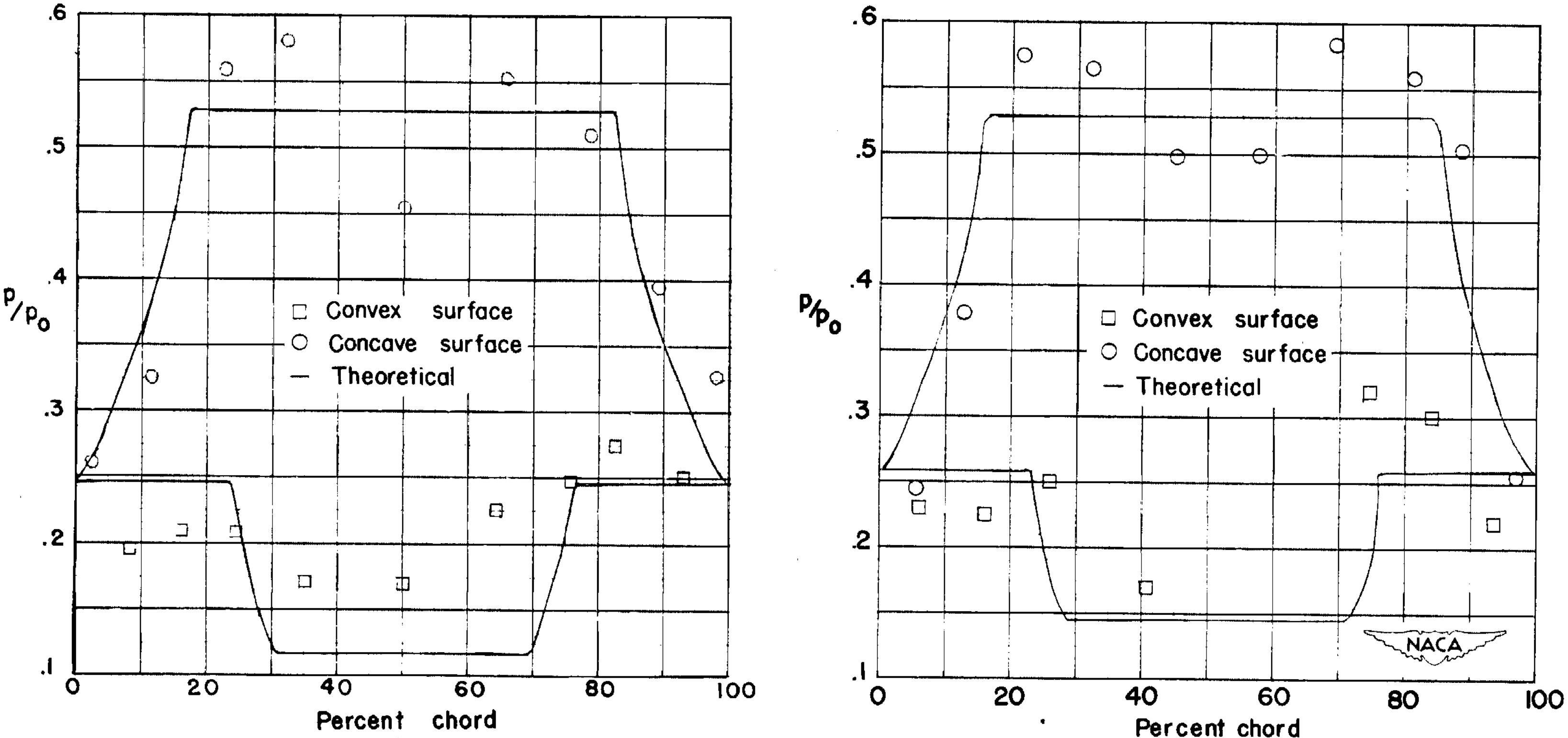

(c) Blade III.

(d) Blade IV.

Figure 17.- Concluded.

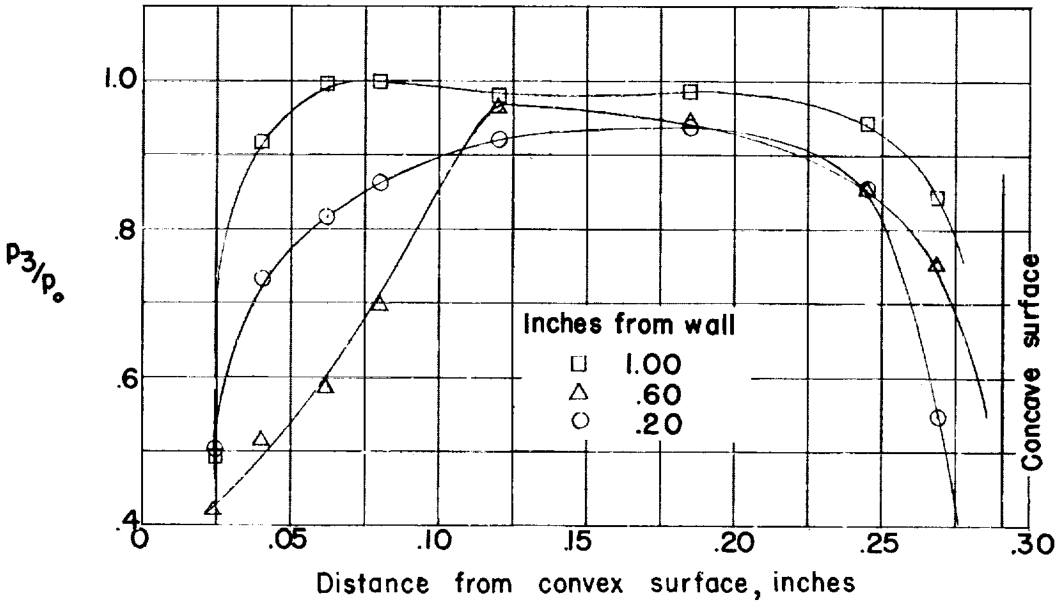

(a) Blade I

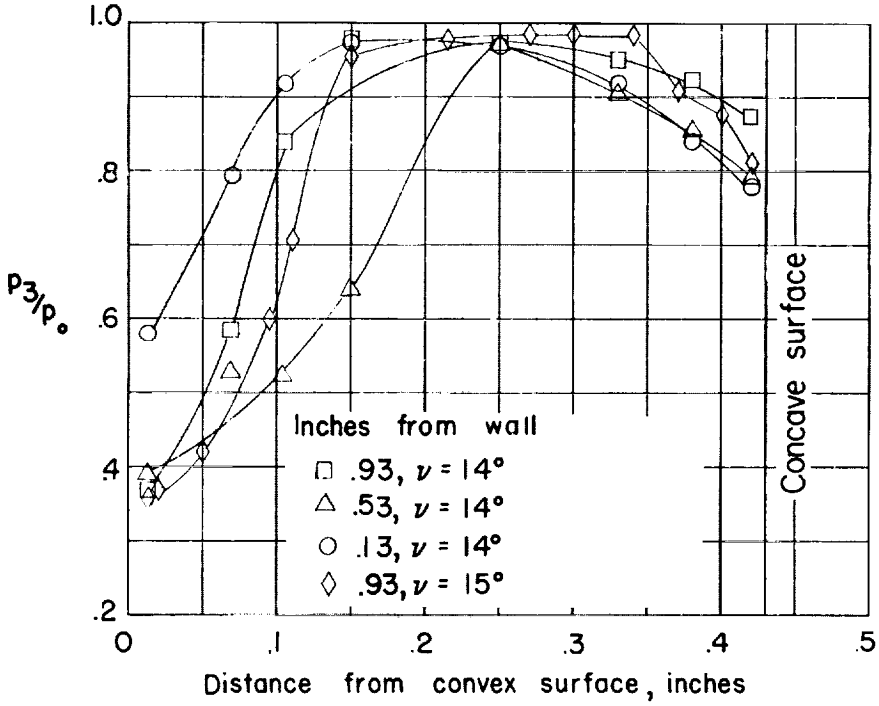

(b) Blade II.

Figure 18.- The variation of the stagnation-pressure recovery near end of passage.

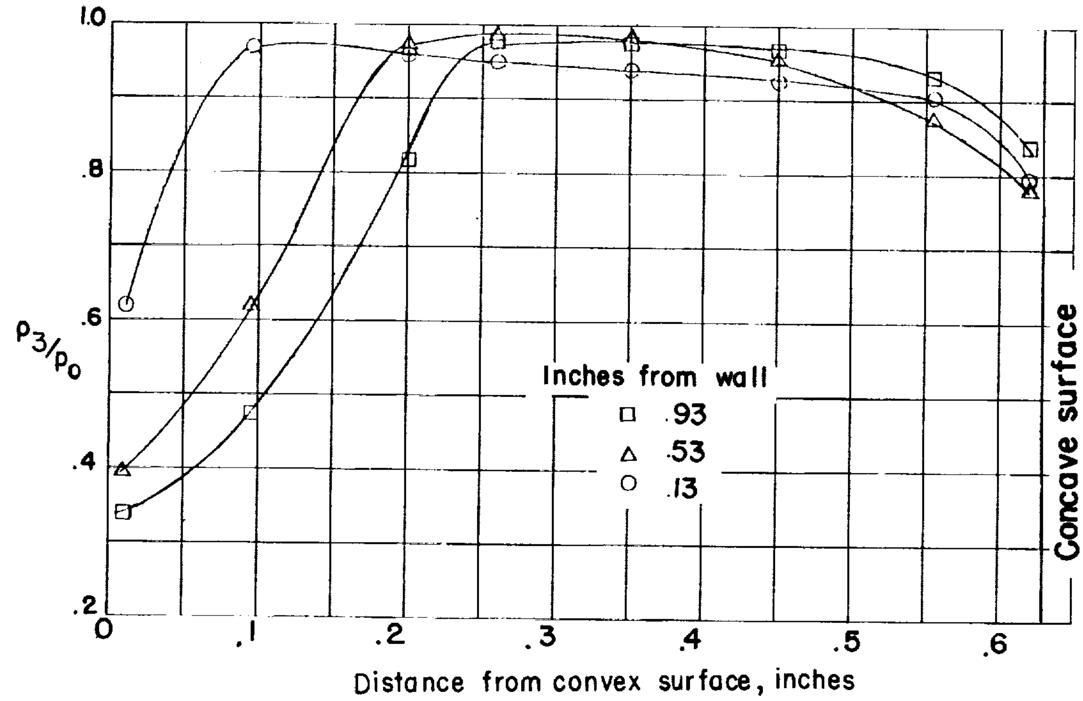

(c) Blade III.

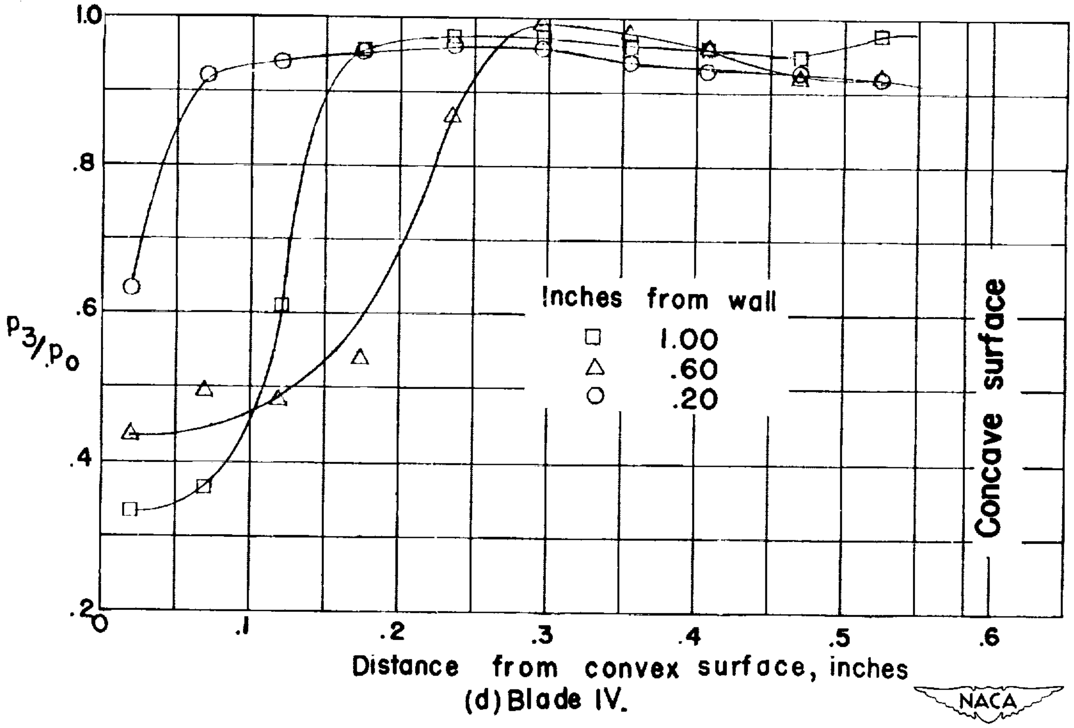

(d) Blade IV.

Figure 18.- Continued.

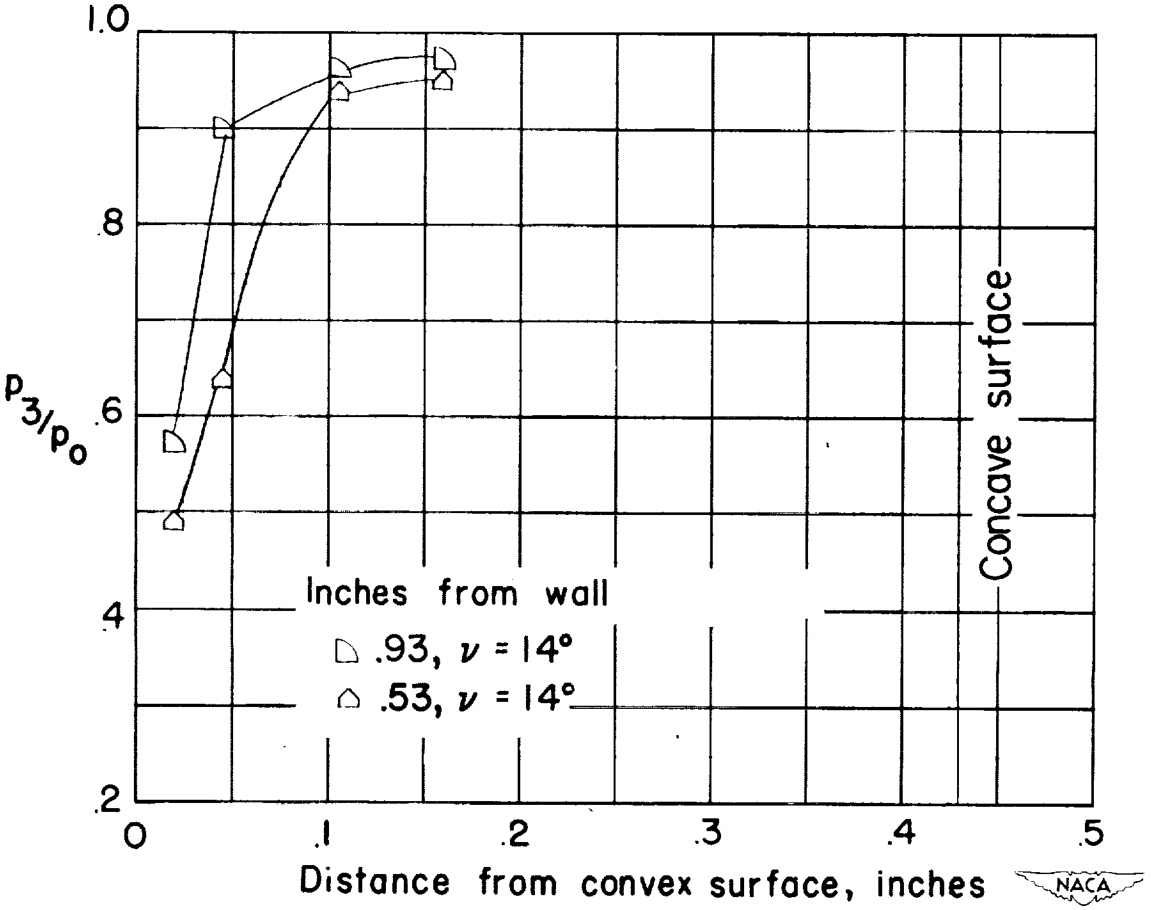

(e) Blade II, with fence.

Figure 18.- Concluded.

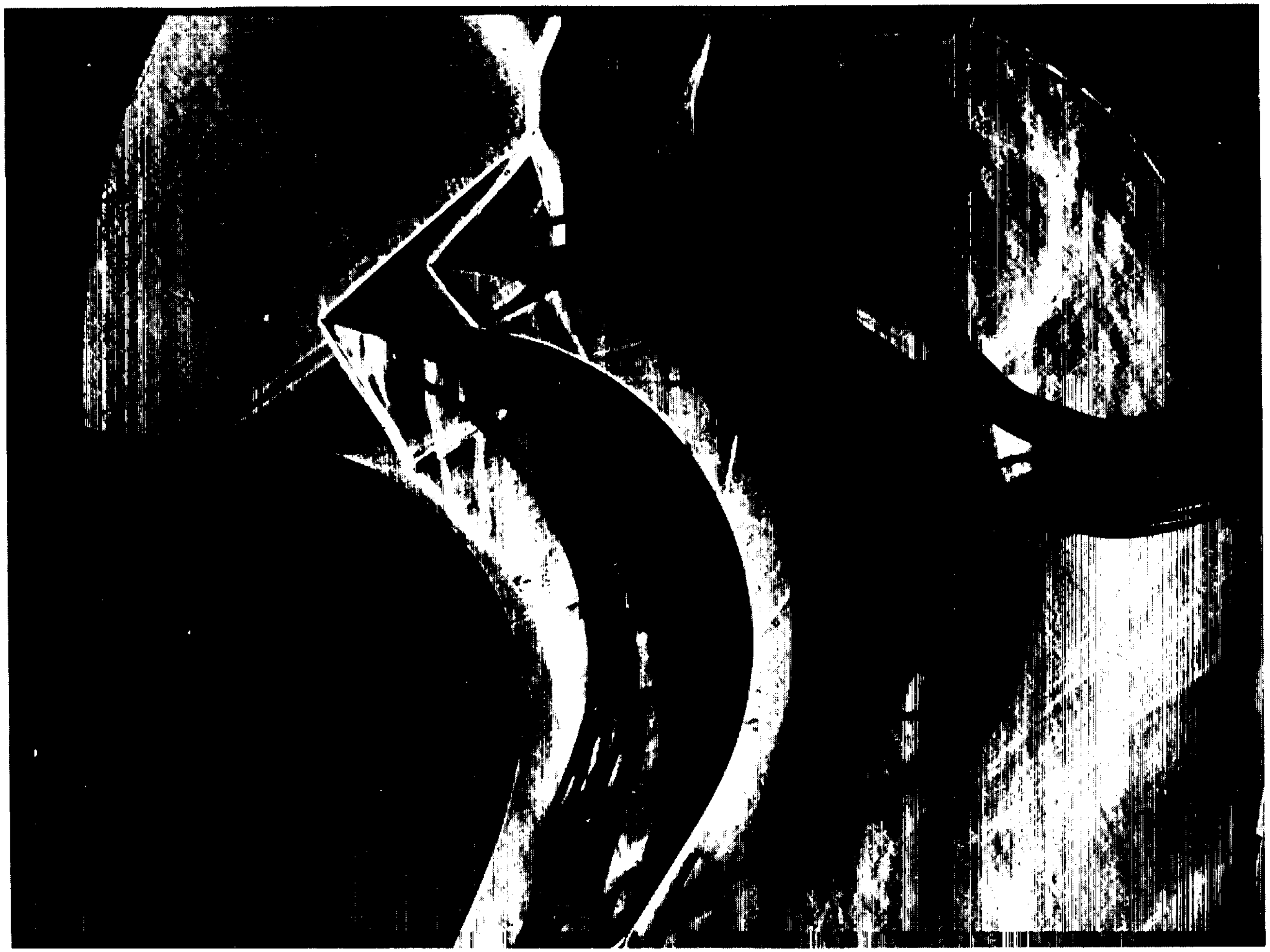

L-72736

(a) Total-pressure tube in place.

Figure 19.- Schlieren photographs of the flow in the passage of blade I. $\nu_e = 15^\circ$.

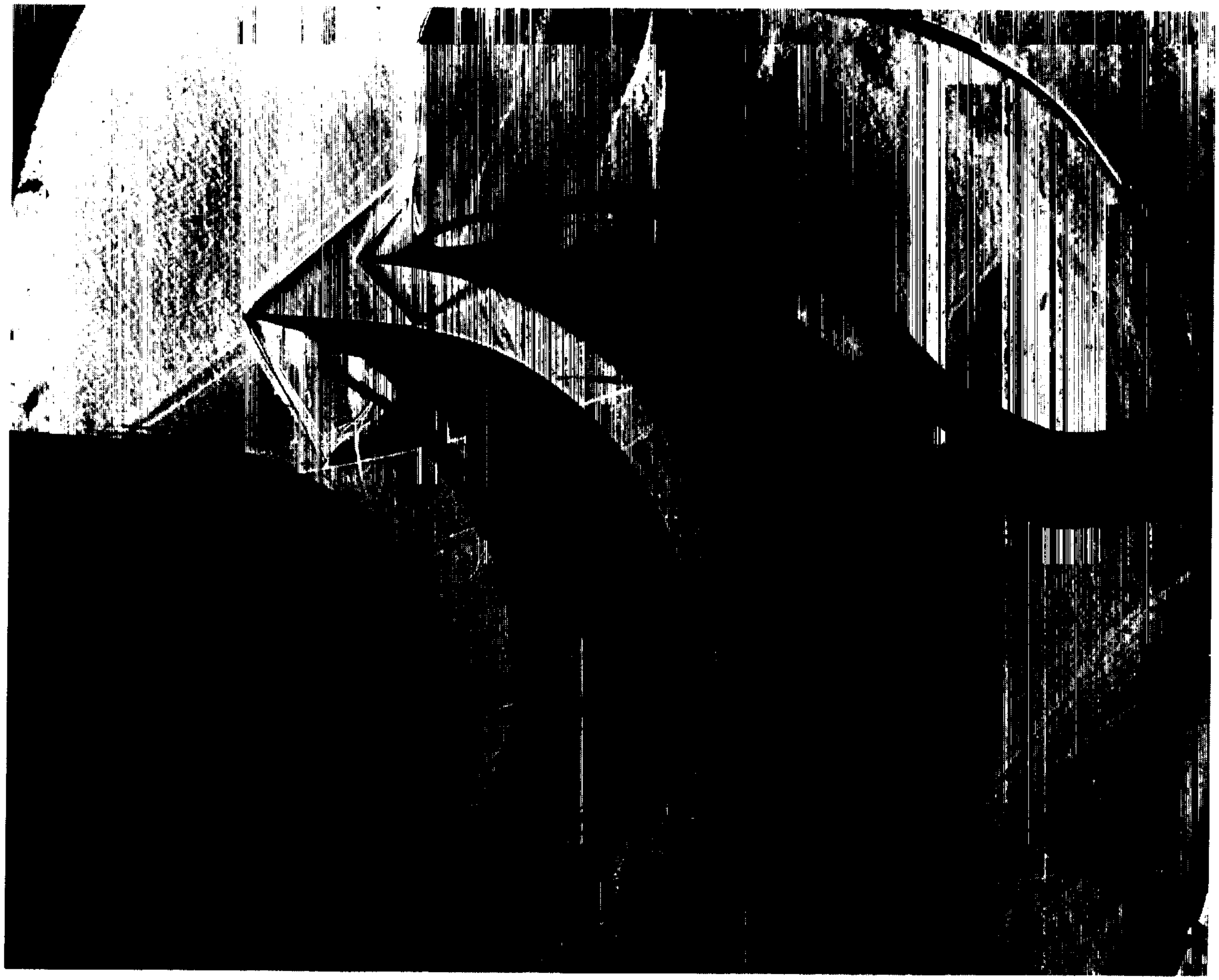

(b) Total-pressure tube removed.

L-72737

Figure 19.- Continued.

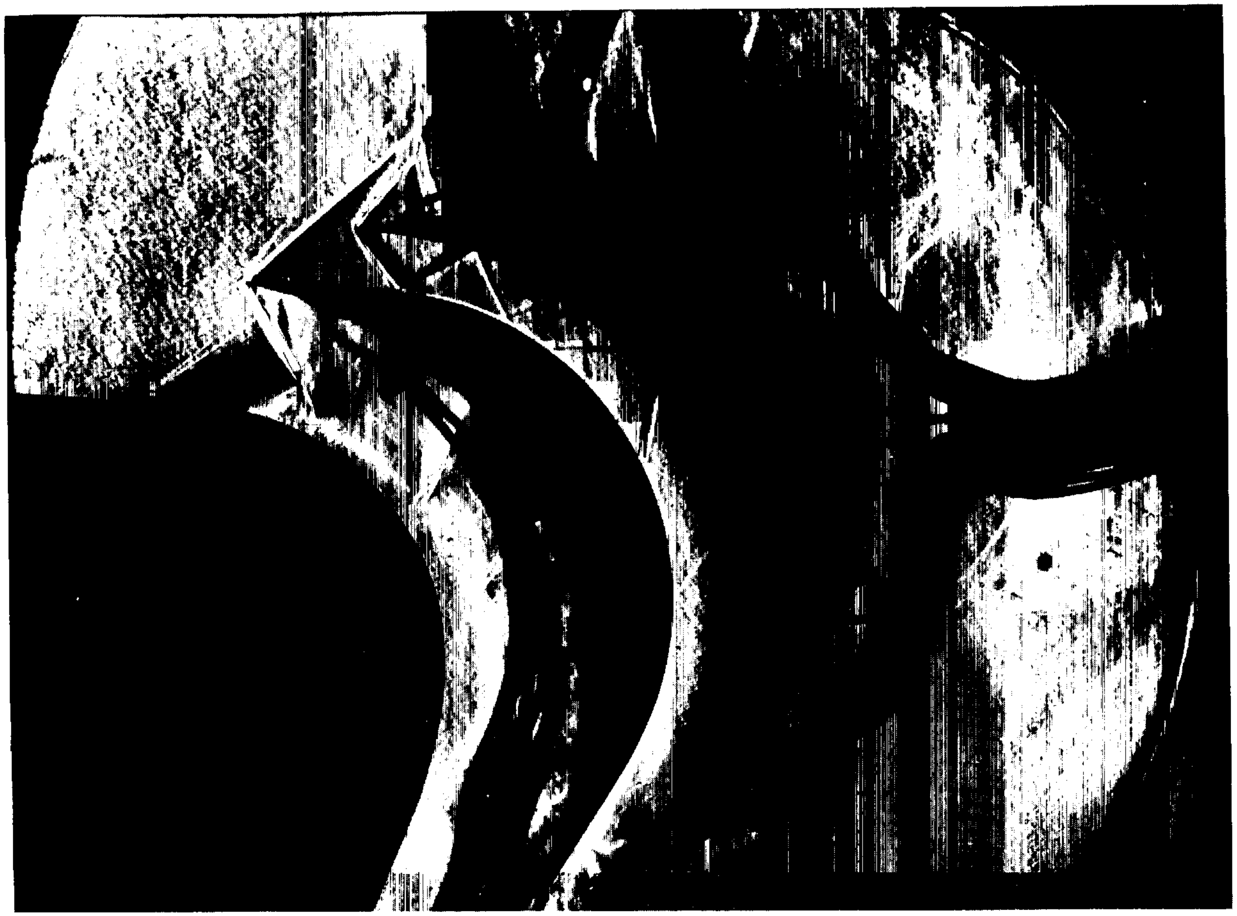

L-72738

(c) Flexible wall moved closer to trailing edge of blades.

Figure 19.- Concluded.

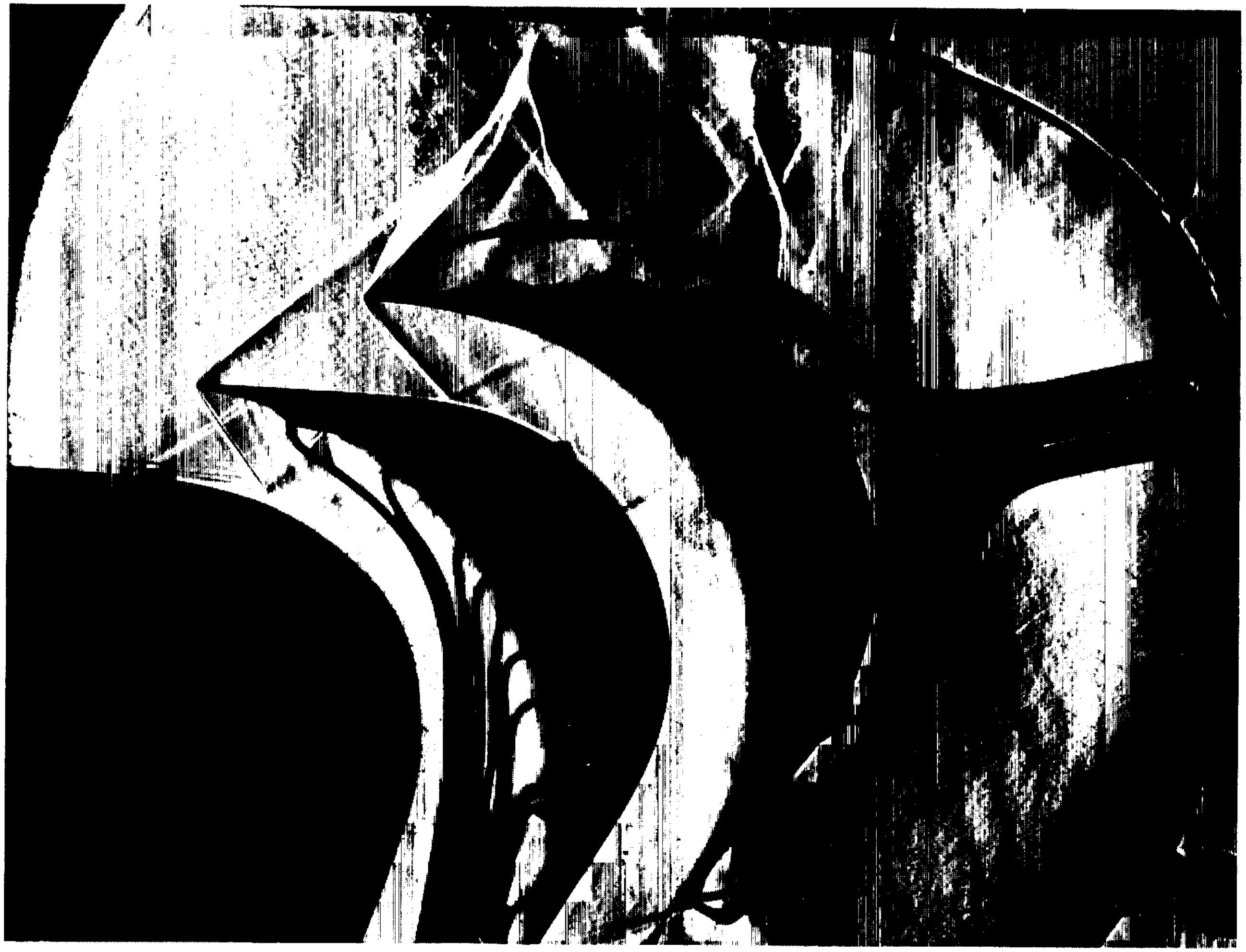

(a) $\nu_e = 14^{\circ}$.

L-72739

Figure 20.- Schlieren photographs of the flow in the passage of blade II.

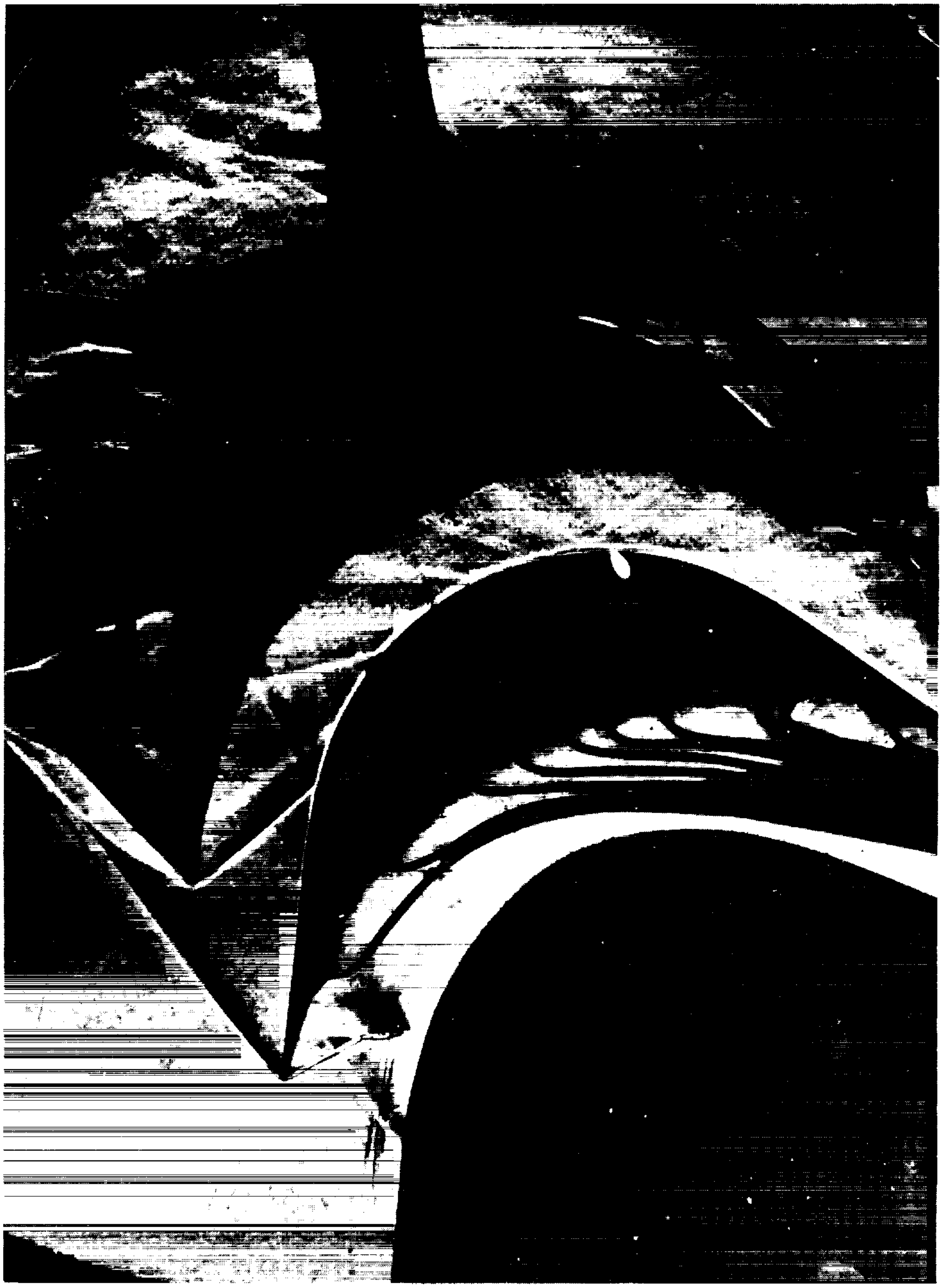

L-72740

(b) $\nu_e = 15^{\circ}$.

Figure 20.- Concluded.

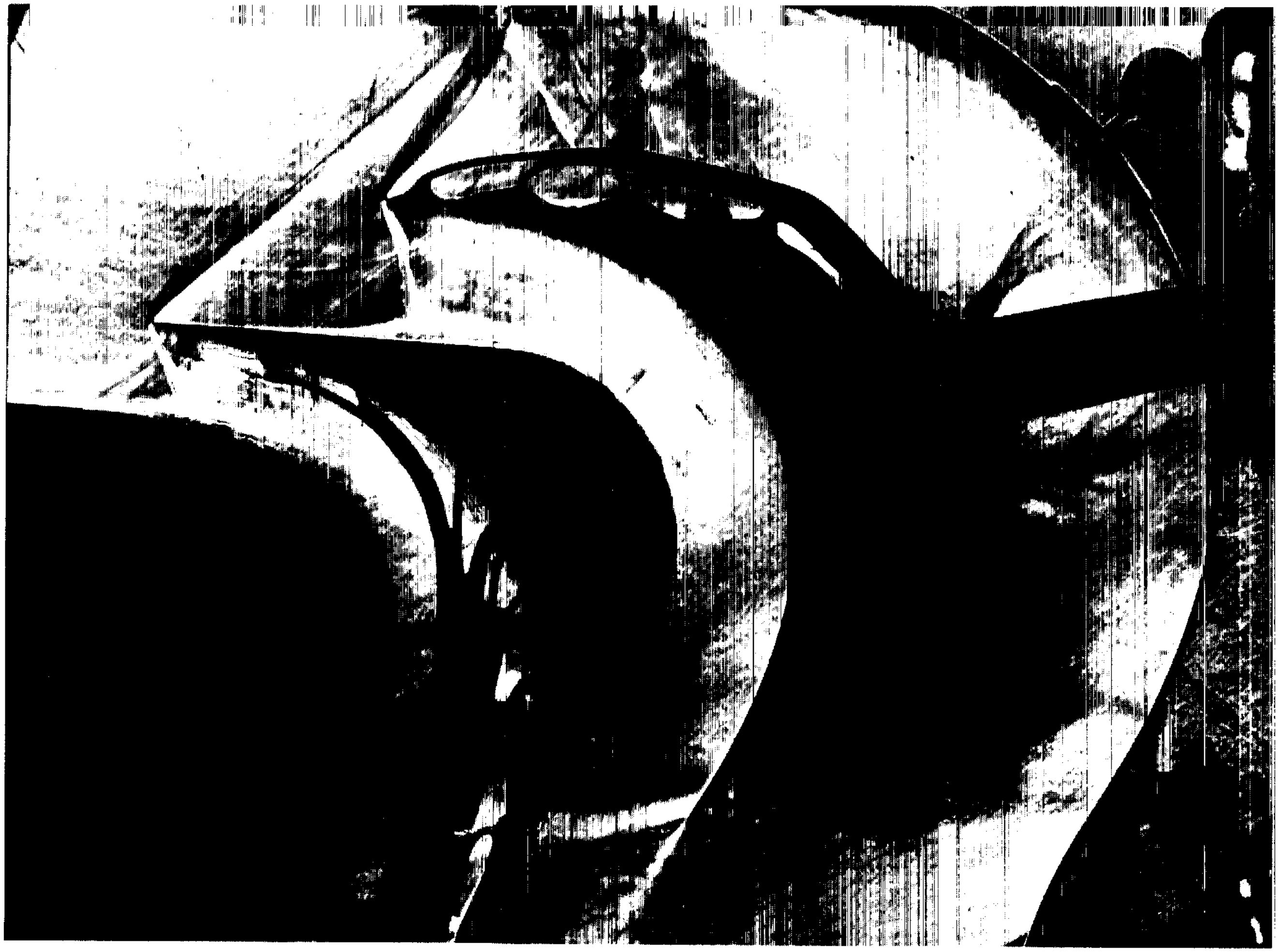

L-72741

(a) Passage not started. $\nu_e = 14^{\circ}$.

Figure 21.- Schlieren photographs of the flow in the passage of blade III.

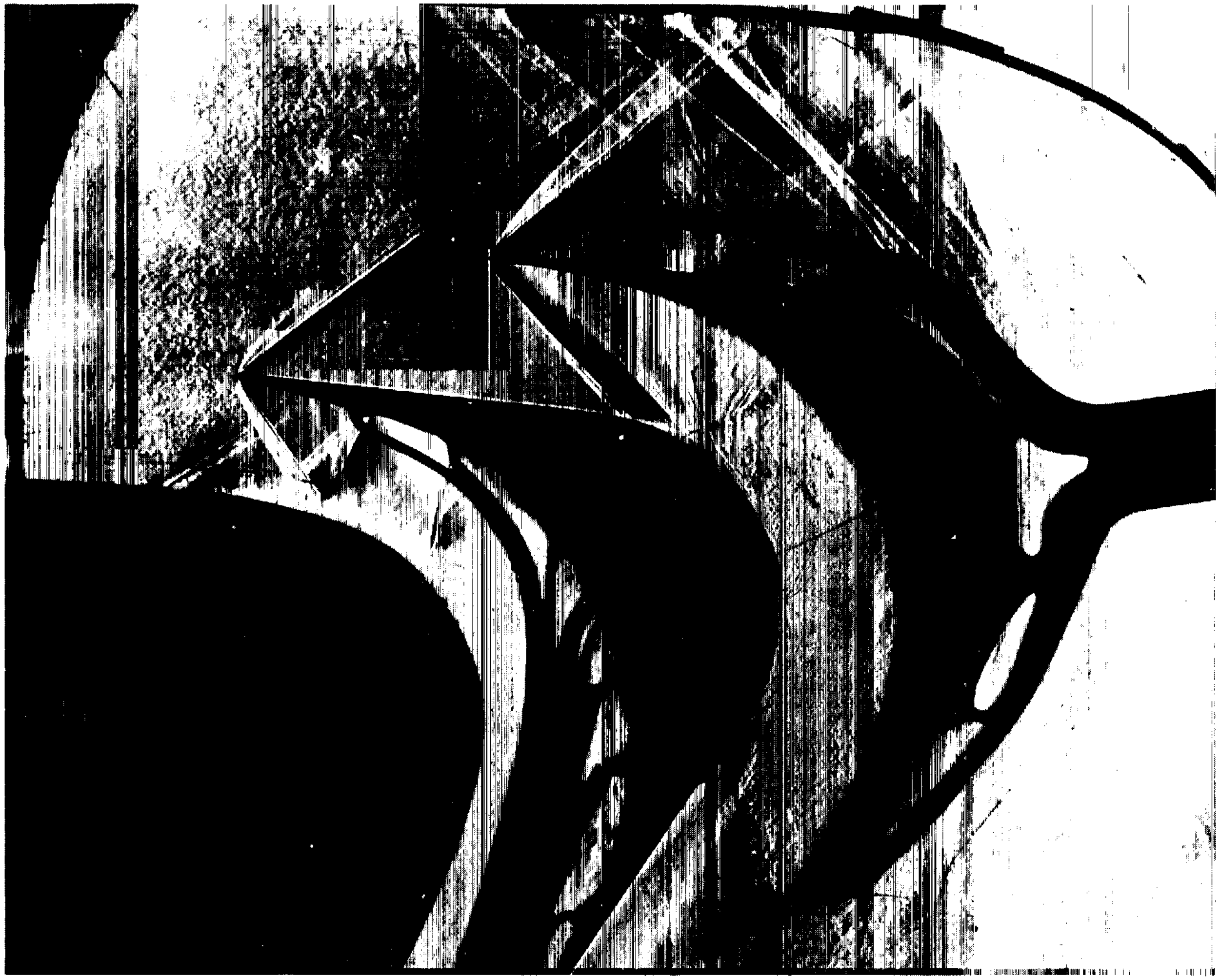

(b) Passage started. $\nu_e = 18^{\circ}$.

Figure 21.- Concluded.

L-72742

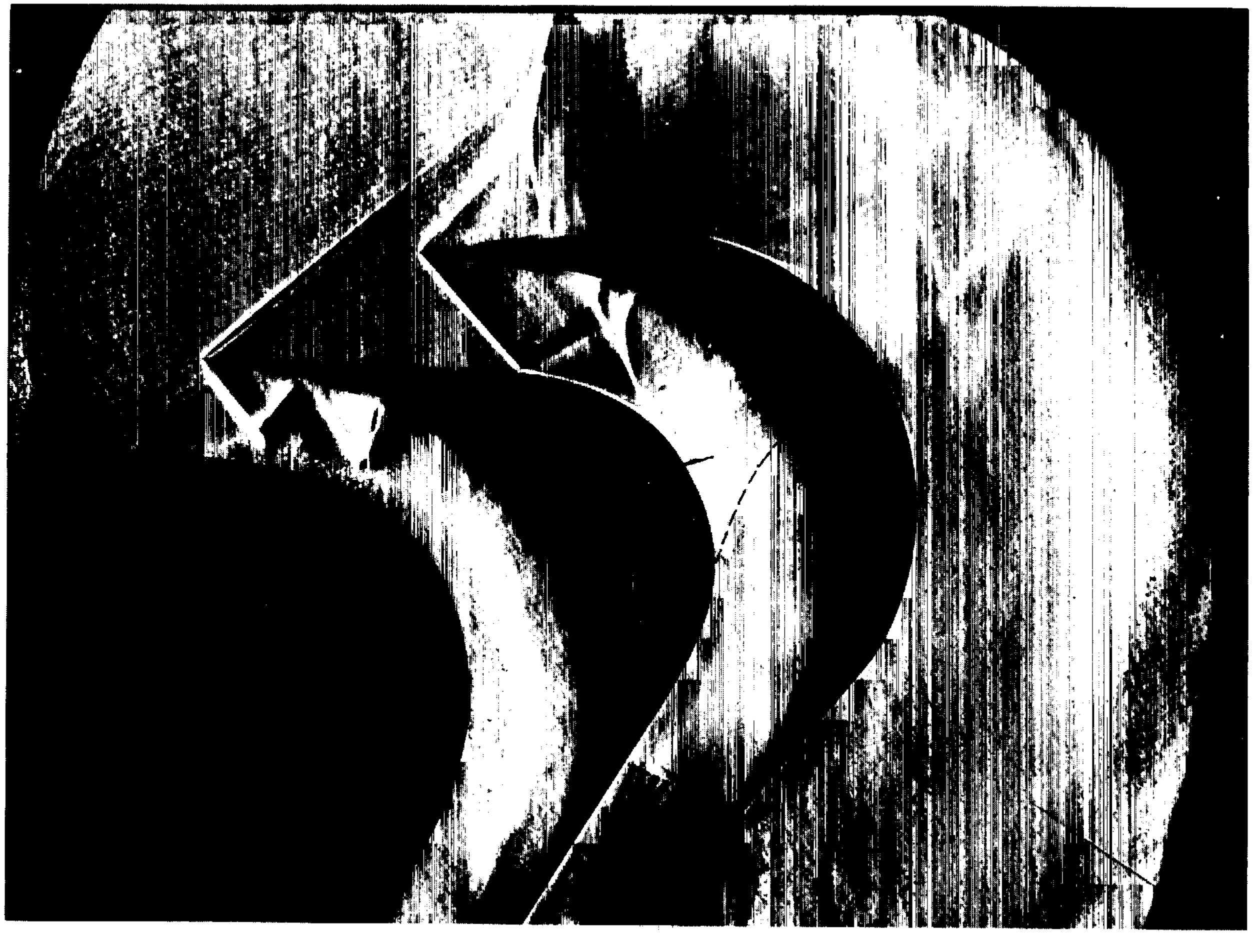

L-72743

Figure 22.- Schlieren photographs of the flow in the passage of blade IV. $\nu_e = 15^\circ$.

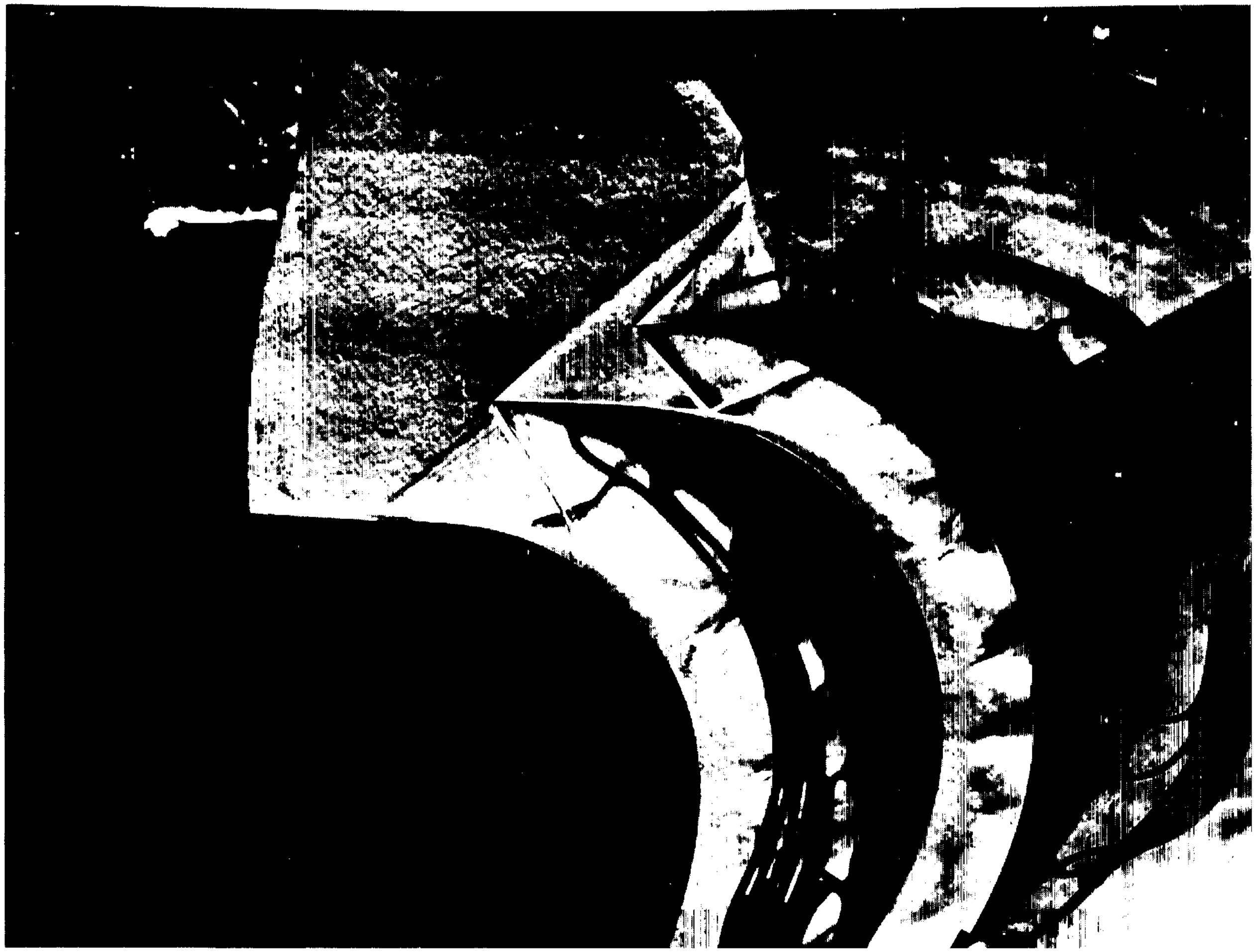

L-72744

Figure 23.- Schlieren photograph of the flow for an incorrectly spaced pair of blades.

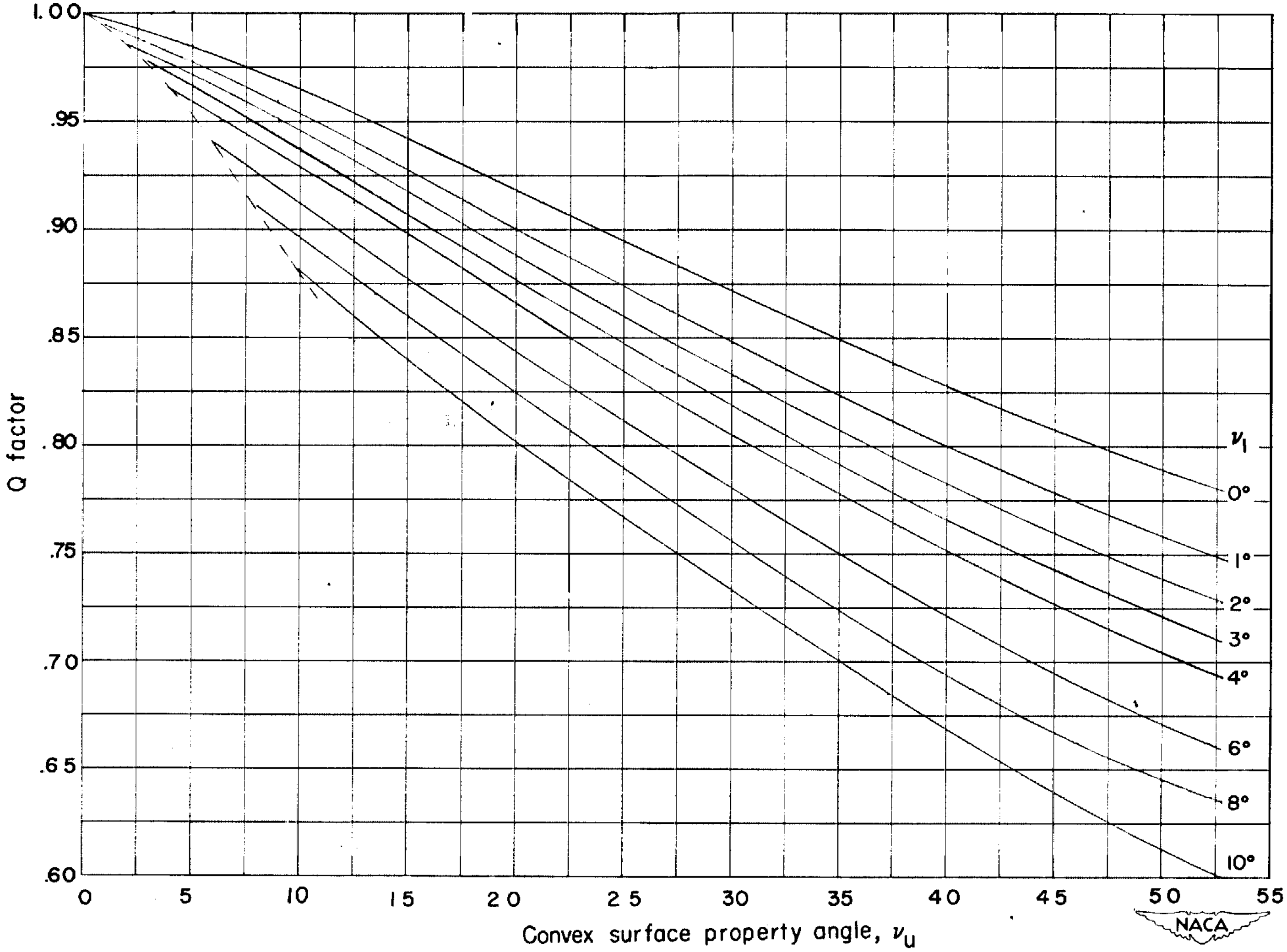

Figure 24.- Q factor for solution of maximum inlet Mach number as a function of ν_u and ν_l.